Modeling of Progressive Damage in the Adhesive Bond Layers of Actuated Plates

D. H. Robbins, Jr.

Dept. of Aerospace Engineering
University of Maryland
College Park, MD, 20742

Email: drobbins@eng.umd.edu

Report Documentation Page		Form Approved OMB No. 0704-0188

Public reporting burden for the collection of information is estimated to average 1 hour per response, including the time for reviewing instructions, searching existing data sources, gathering and maintaining the data needed, and completing and reviewing the collection of information. Send comments regarding this burden estimate or any other aspect of this collection of information, including suggestions for reducing this burden, to Washington Headquarters Services, Directorate for Information Operations and Reports, 1215 Jefferson Davis Highway, Suite 1204, Arlington VA 22202-4302. Respondents should be aware that notwithstanding any other provision of law, no person shall be subject to a penalty for failing to comply with a collection of information if it does not display a currently valid OMB control number.

1. REPORT DATE **30 NOV 2005**	2. REPORT TYPE **N/A**	3. DATES COVERED **-**	
4. TITLE AND SUBTITLE **Adaptive-Hierarchical Modeling of Progressive Damage in Smart Composite Structures**		5a. CONTRACT NUMBER	
		5b. GRANT NUMBER	
		5c. PROGRAM ELEMENT NUMBER	
6. AUTHOR(S)		5d. PROJECT NUMBER	
		5e. TASK NUMBER	
		5f. WORK UNIT NUMBER	
7. PERFORMING ORGANIZATION NAME(S) AND ADDRESS(ES) **U.S. Army Research Office P.O. Box 12211 Research Triangle Park, NC 27709-2211**		8. PERFORMING ORGANIZATION REPORT NUMBER	
9. SPONSORING/MONITORING AGENCY NAME(S) AND ADDRESS(ES)		10. SPONSOR/MONITOR'S ACRONYM(S)	
		11. SPONSOR/MONITOR'S REPORT NUMBER(S)	
12. DISTRIBUTION/AVAILABILITY STATEMENT **Approved for public release, distribution unlimited**			
13. SUPPLEMENTARY NOTES			
14. ABSTRACT			
15. SUBJECT TERMS			

16. SECURITY CLASSIFICATION OF:			17. LIMITATION OF ABSTRACT **UU**	18. NUMBER OF PAGES **53**	19a. NAME OF RESPONSIBLE PERSON
a. REPORT **unclassified**	b. ABSTRACT **unclassified**	c. THIS PAGE **unclassified**			

Standard Form 298 (Rev. 8-98)
Prescribed by ANSI Std Z39-18

Table of Contents

Abstract

This report discusses finite element modeling of progressive damage in the adhesive bond layers of actuated plates and investigates the reduction in actuation capacity caused by the damaged bond layers. The primary challenge posed by this class of problems stems from the vast range of geometric scales that are represented, with the thickness of the adhesive layer representing the smallest scale, the overall thickness of the actuated plate representing the intermediate scale and the in-plane dimensions of the plate representing the largest scale. In multiscale problems, the overall efficiency of the numerical methodology is of paramount importance, thus model development is guided by the need to obtain a sufficiently accurate solution at an acceptable computational expense. In this study, this goal is achieved by through the use of a hierarchical, displacement-based, 2-D finite element model that includes the first-order shear deformation model (FSD), type-I layerwise models (LW1) and type-II layerwise models (LW2) as special cases. Both the LW1 layerwise model and the more familiar FSD model use a reduced constitutive matrix that is based on the assumption of zero transverse normal stress; however, the LW1 model includes discrete layer transverse shear effects via in-plane displacement components that are C^0 continuous with respect to the thickness coordinate. The LW2 layerwise model utilizes a full 3-D constitutive matrix and includes both discrete layer transverse shear effects and discrete layer transverse normal effects by expanding all three displacement components as C^0 continuous functions of the thickness coordinate. The hierarchical finite element model incorporates a 3-D continuum damage mechanics model that predicts local orthotropic damage evolution and local stiffness reduction at the geometric scale represented by the individual material ply or, in the case of layerwise models, by the individual numerical layer. The results clearly demonstrate that the resulting model can efficiently simulate progressive damage in the adhesive layers. For rectangular actuator patches, the adhesive damage is highest near the corners of the actuator and is driven primarily by local concentrations in the transverse normal and transverse shear stresses. In contrast to previous studies that have shown that the inclusion of discrete layer transverse normal stress does not significantly influence the predicted global deformations, the present study shows that the transverse normal stress has a very significant effect in the initiation and progression of localized damage in the adhesive layers.

Keywords: progressive damage, adhesive bonding, debonding, actuated plates, finite elements

List of Figures

Figure 1. (page 7) Idealized nonlinear material behavior. (a) Nonlinearity caused by *plasticity*, (b) Nonlinearity caused by *damage*, and (c) Nonlinearity caused by *plasticity* and *damage*.

Figure 2. (page 8) Representative volume elements showing distribution of microcracks described by damage eigenvalues D_1, D_2 and D_3. D_i is interpreted as the effective fractional reduction in load carrying area due to microcracks that are normal to the ith principal material direction.

Figure 3. (page 15) Progressive damage in an adhesive material under homogeneous deformation and loading. A) Damaged stress/strain curve during imposed simple shear deformation in the 1-3 plane, B) Damage evolution during imposed simple shear deformation in the 1-3 plane, C) Damaged stress/strain curve during imposed uniaxial extension in the 3 direction, D) Damage evolution during imposed uniaxial extension in the 3 direction.

Figure 4. (page 30) A) View of specimen geometry in XY plane and simply supported boundary conditions,   B) Thickness configuration characterized by 2P/H=2 and $2L/h_P$=6, C) Thickness configuration characterized by 2P/H=8 and $2L/h_P$=24.

Figure 5. (page 22) Comparison of adhesive strain distribution near the free corner of the upper actuator patch as predicted by linear elastic LW1 and LW2 models for the case of bending actuation of a simply supported plate.

Figure 6. (page 24) Comparison of adhesive stress distribution near the corner of the upper actuator patch as predicted by linear elastic LW1 and LW2 models for the case of bending actuation of a simply supported plate. Imposed actuation strain in the piezoceramic patch is $\varepsilon_1=\varepsilon_2=0.001$.

Figure 7. (page 26) Comparison of damage distribution in the adhesive layer as predicted by LW1 and LW2 models for the case of bending actuation of a simply supported plate. Imposed actuation strain = 0.001.

Figure 8. (page 28) Comparison of damage distribution in the adhesive layer as predicted by LW1 and LW2 models for the case of bending actuation of a simply supported plate with 2P/H=2 and h_a/h=0.10. Results are shown at four different actuation strain levels.

Figure 9. (page 29) Comparison of stress distribution in the adhesive layer as predicted by LW1 and LW2 models for the case of bending actuation of a simply supported plate with 2P/H=2 and h_a/h=0.10. Results are shown at four different actuation strain levels.

Figure 10. (page 30) Comparison of stress distribution in the adhesive layer as predicted by linear elastic and progressive damage solutions obtained with LW1 and LW2 models.

Results shown for a simply supported plate subjected to bending actuation (actuation strain = 0.001). 2P/H=2 and h_a/h=0.10.

Figure 11. (page 31) Comparison of damage distribution in the adhesive layer as predicted by LW1 and LW2 models for the case of bending actuation of a simply supported plate with 2P/H=8 and h_a/h=0.10. Results are shown at four different actuation strain levels.

Figure 12. (page 32) Comparison of stress distribution in the adhesive layer as predicted by LW1 and LW2 models for the case of bending actuation of a simply supported plate with 2P/H=2 and h_a/h=0.10. Results are shown at four different actuation strain levels.

Figure 13. (page 33) Comparison of stress distribution in the adhesive layer as predicted by linear elastic and progressive damage solutions obtained with LW1 and LW2 models. Results shown for a simply supported plate subjected to bending actuation (actuation strain = 0.001). 2P/H=8 and h_a/h=0.10.

Figure 14. (page 35) Normalized center deflection produced by constant bending actuation (actuation strain = 0.001) followed by an opposing uniform distributed transverse load.

Figure 15. (page 36) Comparison of damage distribution in the adhesive layer as predicted by LW1 model (Parts A & B) and LW2 model (Parts C & D). Uniform distributed transverse load increments (1 MPa each) are applied to oppose pre-existing bending actuation (actuation strain = 0.001)

Figure 16. (page 37) Comparison of stress distribution in the adhesive layer as predicted by LW1 and LW2 models. Uniform distributed transverse load increments (1 MPa) are applied to oppose pre-existing bending actuation (actuation strai=0.001). 2P/H=2, h_a/h=0.10.

Figure 17. (page 38) Comparison of stress distribution in the adhesive layer as predicted by linear elastic and progressive damage solutions obtained with LW1 and LW2 models. Results shown for a simply supported plate subjected to combined bending actuation (actuation strain = 0.001) and opposing uniform distributed transverse load (4 MPa). 2P/H=2 and h_a/h=0.10.

Figure 18. (page 39) Comparison of damage distribution in the adhesive layer as predicted by LW1 and LW2 models. Uniform distributed transverse load increments (0.0625 MPa) are applied to oppose pre-existing bending actuation (actuation strain = 0.001). 2P/H=8, h_a/h=0.10.

Figure 19. (page 40) Comparison of stress distribution in the adhesive layer as predicted by LW1 and LW2 models. Uniform distributed transverse load increments (0.0625 MPa) are applied to oppose pre-existing bending actuation (actuation strain = 0.001). 2P/H=8, h_a/h=0.10.

Figure 20. (page 40) Comparison of stress distribution in the adhesive layer as predicted by linear elastic and progressive damage solutions obtained with LW1 and LW2 models. Results shown for a simply supported plate subjected to combined bending actuation (actuation strain = 0.001) and opposing uniform distributed transverse load (0.375 MPa). $2P/H=8$ and $h_a/h=0.10$.

Figure 21. (page 42) Damage and transverse stress distribution in the lower adhesive bond layer for simply supported actuated plate subjected to uniform distributed transverse load with passive actuators.

List of Tables

1. Introduction and Background

As evidenced by the large number of works cited in the recent reviews by Benjeddou (2000) and Chopra (2002), there have been extensive efforts to develop analytical models and finite element models of laminated composite structural components (i.e. beams, plates, and shells) that contain surface-mounted or embedded piezoelectric actuators and/or sensors. On a purely mechanical basis, these modeling efforts can be broadly classified into two basic categories according to the kinematics assumed by each model.

The first category of models, known as 'equivalent single layer' models (or ESL models), are distinguished by the use of a displacement field that exhibits C^1 continuity with respect to the laminate thickness coordinate, i.e., the displacement components and their thickness derivatives are continuous through the entire laminate thickness dimension. The primary advantage of the ESL models is their high level of computational efficiency which stems from the fact that very few functions need to be determined in order to completely define the displacement field. However, despite the fact that ESL model solutions are computationally expedient, the basic assumption of a C^1 thickness continuity of the displacement field is overly restrictive and, as discussed by Robbins and Chopra (2006), poses two major difficulties in the modeling of actuated plates. First, the continuous thickness derivatives of the displacement components prevent the ESL models from delivering accurate ply-level stress and strain fields for laminates where adjacent material layers differ significantly in their mechanical properties and thicknesses. Second, the ESL models cannot accurately represent the diversion of actuation energy into localized transverse shear deformation near the edges of the actuators; consequently, the ESL models consistently over-predict the global deformation of the actuated plate caused by the actuators.

Early efforts at developing ESL models of actuated plates were essentially adaptations of the classical laminate theory (or CLT) that is based on the Kirchhoff assumption that transverse normal material fibers remain straight and normal to the curved midplane of the structural component. Within the CLT framework, piezoelectrically actuated beam models were developed by Crawley and deLuis (1987), while early actuated plate and actuated shell models were developed by Lee (1990) and Tzou and Gadre (1989) respectively. For slightly thicker laminates, the first order shear deformation theory (FSD) provides macroscopic ESL kinematics that are more appropriate since it permits a rudimentary gross shear deformation that is assumed constant with respect to the thickness coordinate. FSD finite element models of piezoelectrically actuated beams, plates, and shells were developed by Robbins and Reddy (1991), Lin et al. (1996), and Miller and Abramovich (1995). Higher order ESL models with full thermo-electro-mechanical coupling were developed for quasi-static analysis by Chattopadhyay et al. (1999) and for dynamic analysis by Zhou et al. (2000). In both of these studies, the in-plane displacement components were assumed to be cubic functions of the thickness coordinate, while transverse normal effects were neglected via the assumption of zero transverse normal stress.

The second category of models, known as 'discrete layer' models (or layerwise models), are distinguished by the use of a displacement field that exhibits only C^0 continuity with respect to the laminate thickness coordinate, i.e., the displacement components themselves are continuous through the entire laminate thickness dimension, but their thickness derivatives are permitted to exhibit one or more discontinuities commensurate with the level

of transverse discretization employed. In practical terms, layerwise models discretize the laminate thickness dimension into a contiguous set of numerical layers. The displacement field is then separately defined within each numerical layer in such a way that the displacement components maintain continuity across interlayer boundaries; however their thickness derivatives are not required to be continuous across the interlayer boundaries. Provided that the number of numerical layers is greater than or equal to the number of distinct material layers, the layerwise displacement field is capable of correctly representing the kinking and warping of transverse normal fibers that is commonly observed in multilayer laminates. This particular modeling capability becomes especially important in actuated plates due to the presence of adhesive bond layers that are typically much more compliant than the structural substrate material or the actuator material.

It should be emphasized that full 3-D finite element models are classified as discrete layer models provided that more than one 3-D element is used to discretize the laminate thickness dimension. If, on the other hand, the entire thickness dimension of the laminate is encompassed in a single layer of 3-D finite elements, then the resulting model is effectively an ESL model.

Reddy (1987, 1989) generalized the layerwise concept by expanding the laminate displacement field through the thickness in terms of a 1-D Lagrangian finite element interpolation where both the number of 1-D elements and the polynomial order of the 1-D interpolation functions are arbitrary. This data structure provides a very convenient framework from which to develop layerwise finite element models of beams, plates and shells. A layerwise model for piezoelectrically actuated beams was first reported by Robbins and Reddy (1991) who used an induced strain approach to approximate the piezoelectric effect (i.e. similar to imposing a temperature change in the piezoelectric material only). Saravanos and Heyliger (1995) developed a layerwise beam model with fully coupled electrical and displacement fields. Both these studies clearly demonstrated that fundamental differences exist between the predicted solutions from layerwise models and ESL models. A layerwise composite plate model was reported by Robbins and Reddy (1993), once again using an induced strain approach to approximate the piezoelectric effect. They demonstrated that the resulting layerwise plate model produced laminate solutions that were equivalent to 3-D finite element solutions provided that comparable levels of discretization were used. Heyliger, et al. (1994) and Saravanos, et al. (1997) developed layerwise plate models with full electro-mechanical coupling. Lee and Saravanos (1997) extended the layerwise plate model to include thermo-electro-mechanical coupling, while Saravanos (1997) developed a layerwise shell model with electro-mechanical coupling. In addition to layerwise finite element solutions, exact 3-D elasticity solutions have been obtained for relatively simple problems by Heyliger (1997) and Gopinathan, et al. (2000).

The material heterogeneity of multilayer actuated structural components inevitably gives rise to stress concentrations which typically occur at the intersection of material interfaces and free edges. These stress concentrations primarily involve the transverse shear stress and transverse normal stress and are most pronounced near the edges of the thin adhesive layer where they serve to transfer the load from the actuator to the underlying structural substrate, or vice-versa in the case of a bonded sensor (Robbins and Reddy, 1996; Vel and Batra, 2000; Zhang et al., 2003). These locally elevated transverse stresses are particularly important since they are likely to cause damage to the

adhesive material which could become severe enough to compromise the overall functionality of the actuator or sensor.

Despite the obvious importance of this particular issue, there have been no reported efforts to predict the evolution of damage within the adhesive bond layers of actuated structural components. However, there has been considerable research effort in developing numerical methods to predict damage accumulation in fiber-reinforced composite laminates, and in the present study, this body of knowledge is leveraged in developing a numerical methodology to predict damage evolution in actuated structural components.

Most of the past efforts to model the evolution of distributed microscopic damage in fiber-reinforced composite laminates have relied on the use of continuum damage mechanics (or CDM). CDM is distinguished by the introduction of an internal tensor field (i.e. the damage tensor) that describes the distribution, density and orientation of microcracks (Krajcinovic, 1996; Lemaitre, 1996; Skrzypek and Ganczarski, 1999). The evolution of the damage tensor and the resulting reduction of material stiffness are described within the framework of irreversible thermodynamics.

Early efforts to apply CDM to composite laminates (e.g., Talreja, 1985; Lene, 1986; Allen et al., 1987a,b; and Lee et al., 1989) focused mainly on the development of a suitable form for the damage variable and expressing the stiffness degradation in terms of the chosen damage variable. Talreja (1985) chose a set of vectors to represent microcrack densities on various directed planes in the pre-homogenized composite material, while Lene (1986) used a scalar quantity to describe the degree of fiber/matrix debonding in the heterogeneous microstructure prior to homogenization. In both of these works, the damage evolution equations received minimal or no treatment. Allen et al. (1987a,b) and Lee et al. (1989) developed a progressive damage model of laminated composites using damage dependent constitutive relations for the homogenized composite material at the ply level. Distributed microscopic damage was quantified using an internal variable (2nd order tensor) that represented additional strain that results from the presence of damage; however, the damage evolution law was empirically based, instead of being derived from a free energy function. The model accounted for matrix cracking and fiber fracture for laminates subjected to monotonic and cyclical uniaxial loading.

Ladeveze and co-workers (e.g., Ladeveze and Dantec, 1992; Allix and Ladeveze, 1989,1992; Ladeveze et al., 2000) developed a mesomechanical model where damage is predicted independently for each homogenized composite ply and each interface that separates adjacent plies. The in-plane damage modes are assumed to be uniformly distributed through the thickness of each homogenized composite ply and are described by three internal variables that define the reduction in the in-plane stiffnesses E_{11}, E_{22} and G_{12}. The transverse damage mode is restricted to the 2-D interfaces separating adjacent plies and is described by an additional internal variable that effectively defines the reduction in transverse normal and transverse shear stiffnesses E_{33}, G_{13}, G_{23}. The damage variables are assumed to have simple evolution laws that are derived from a free energy function.

Voyiadjis and coworkers (e.g., Voyiadjis and Kattan, 1993, 1999; Voyiadjis and Park, 1999; Voyiadjis and Delikas, 2000) developed a 3-D model for coupled progressive damage and plasticity based on the use of a symmetric second order damage tensor

whose the eigenvectors represent the principal directions of damage and whose eigenvalues represent the density of distributed microcracks that are normal to the respective eigenvectors. Damage is predicted separately for the fiber and matrix constituents followed by homogenization of the damaged microstructure. Although rigorously formulated using a three-step split operator algorithm to separate the deformation into elastic, plastic and damage components, the resulting model appears to be quite computationally intensive, hence its suitability for large scale simulation is questionable.

Barbero and De Vivo (2001) developed a 2-D (plane stress) model for progressive damage based on the use of a symmetric second order damage tensor whose eigenvalues represent the density of distributed microcracks oriented normal to the principal material coordinate directions. This assumption regarding the form of the damage tensor permits considerable simplification in the overall implementation of damage mechanics while still maintaining a sufficient level of generality to adequately describe the observed behavior of fiber reinforced composite laminates. In addition, damage evolution and stiffness reduction are computed for the pre-homogenized composite material which further simplifies the formulation. The model was extended by Barbero and Lonetti (2002) to include plasticity, and further extended by Lonetti et al. (2003) to include triaxial orthotropic damage in terms of three damage eigenvalues. Lonetti et al. (2003) used the triaxial damage model in conjunction with 3-D finite elements that each span the entire thickness of the laminate thus encompassing all of the material layers in a single element.

Robbins et al. (2005) discussed the numerical treatment of 3-D continuum damage mechanics within the context of a macroscopic finite element model based on the first order shear deformation theory of laminates. The authors studied the effect of various modeling parameters on predicted damage evolution and global failure. These parameters included 2-D mesh density, 2-D element type (i.e. polynomial order), element integration scheme and element distortion level. The progressive damage solution was shown to exhibit convergence with increasing mesh density and was furthermore shown to exhibit minimal sensitivity to changes in the remaining modeling parameters. Robbins and Reddy (2006) compared the damage predictive capabilities of ESL models and layerwise models, and concluded that ESL models consistently under-predict local damage evolution and consistently over-predict global failure loads due to the inability of ESL models to correctly resolve the transverse shear stress maxima.

2.   Objectives and Methods

While a review of the literature reveals numerous studies devoted to finite element modeling of the response of actuated plates, the issue of structural integrity of such composite systems has received very little attention to date, despite the fact that this particular concern has been raised in numerous papers. The material mismatches that are inherent in actuated plates give rise to severe stress concentrations that are likely to cause material damage, particularly in the adhesive layer used to bond the actuator or sensor to the structural substrate. While there have been a few studies that have investigated the effect of damaged adhesive bonds on the overall functionality of actuated plates, the adhesive damage itself was assumed, not predicted (Sun et al., 2001; Kim and Jones,

1996). To date, there have been no reported efforts to predict the mode, severity and extent of adhesive damage that occurs during the application of anticipated service loads.

In response to this deficiency, the overall objective of the present study is to develop and demonstrate a finite element methodology that is capable of modeling progressive damage in adhesive bond layers of actuated plates. This finite element methodology is used to investigate the mode, severity and extent of distributed microscopic damage that accumulates in the adhesive bond layers of a simply-supported actuated plate that is subjected to bending actuation and/or distributed transverse loading. In addition, the study quantifies the relative contributions to adhesive damage from transverse shear deformation and transverse normal deformation, and further quantifies the effect of the 'predicted' adhesive damage on the overall functionality of the actuated plate.

The computational model that is used to accomplish these goals is developed by incorporating a 3-D continuum damage mechanics model into a hierarchical, displacement-based finite element model that is specifically formulated to facilitate the simulation of composite laminate behavior.   The hierarchical finite element formulation is ideally suited for the present study since it permits the assumed kinematics of the entire model (or any given element) to be easily changed. This feature is particularly relevant for the present focus problem where the effect of kinematic assumptions on predicted adhesive damage is not well understood.   The hierarchical model includes the first-order shear deformation model (FSD), type-I layerwise models (LW1) and type-II layerwise models (LW2) as special cases.   Both the LW1 layerwise model and the more familiar FSD model use a reduced constitutive matrix that is based on the assumption of zero transverse normal stress; however, the LW1 model also includes discrete layer transverse shear effects via inplane displacement components that are C^0 continuous with respect to the thickness coordinate.   The LW2 layerwise model utilizes a full 3-D constitutive matrix and includes both discrete layer transverse shear effects and discrete layer transverse normal effects by expanding all three displacement components as C^0 continuous functions of the thickness coordinate.

Since the prediction of local damage evolution requires the use of a macroscopic model that is capable of delivering accurate 3-D stress and strain distributions within each constituent material of the actuated plate, the use of a first order shear deformation (FSD) model is not appropriate for the task (Robbins and Reddy, 2006); consequently, all simulations in the present study are performed using layerwise finite elements.

The particular 3-D continuum damage model used in this study is not intended to be novel; rather, it is simply intended to be representative of the many published damage models that have been discussed in the literature for predicting damage evolution and stiffness reduction in composite laminates. For completeness sake, the development of the 3-D damage model is fully described in this paper and shares many similarities with the developments found in Barbero and De Vivo (2001) and Lee et al. (1985). The numerical implementation of this particular damage model is described in detail by Robbins et al. (2005) and Robbins and Reddy (2006).

It should be emphasized that the objective of this problem is not necessarily to produce a solution that agrees very closely with experimental results, but rather to demonstrate that the present methodology is adequate for such simulations and can be used to investigate the fundamental characteristics of localized adhesive bond damage and its impact on the overall functionality of the actuated plate. In order to differentiate

the relative contributions to local adhesive damage from transverse shear deformation and transverse normal deformation, both the LW1 and LW2 layerwise models are used to obtain solutions. The scope of the present study is restricted to the prediction of progressive damage and local material failure that occur in the adhesive bond layers of actuated plates under quasi-static, monotonic increasing load conditions.

The remainder of the paper is organized as follows. In Section 3, the 3-D continuum damage mechanics model is developed for the special case of orthotropic damage, culminating in the damaged constitutive relations and the governing equations that drive the evolution of the internal damage variable. Section 4 describes the hierarchical laminate model that is used to produce the series of macroscopic models that are used in the study. Section 4 also contains a brief description of the numerical implementation of the 3-D continuum damage mechanics model into the hierarchical macroscopic finite element model. In Section 5, numerical examples are presented to demonstrate the fundamental characteristics of adhesive damage predicted by the model. Finally, concluding remarks are given in Section 6.

3.   3-D continuum damage mechanics model

On the microscopic scale, damage is characterized by molecular bonds that have been broken and are no longer available to support loads. As damage accumulates, the molecular bond density of the material decreases, resulting in a reduction of stiffness and consequently a nonlinear (softening) stress/strain relationship. Typically these broken bonds are not uniformly distributed in the material, tending instead to nucleate into microcracks and microvoids. Figure 1 illustrates the phenomenological differences between the nonlinear softening material behavior that occurs in the case of progressive damage and the more familiar case of plasticity. The plastic behavior shown in Figure 1a is associated with the development of slip planes that cause a permanent plastic strain ε_p. However, the plastic flow does not affect the bond density of the material, and consequently the material does not experience a permanent reduction in stiffness. In contrast, the nonlinear behavior in Figure 1b is due solely to damage (without plastic flow) and thus exhibits a permanent reduction in stiffness. However, upon removal of the loads, the damaged material does not exhibit a permanent deformation. Figure 1c shows nonlinear material behavior that is caused by both plasticity and damage, and consequently exhibits both a permanent plastic strain and a permanent reduction in stiffness.
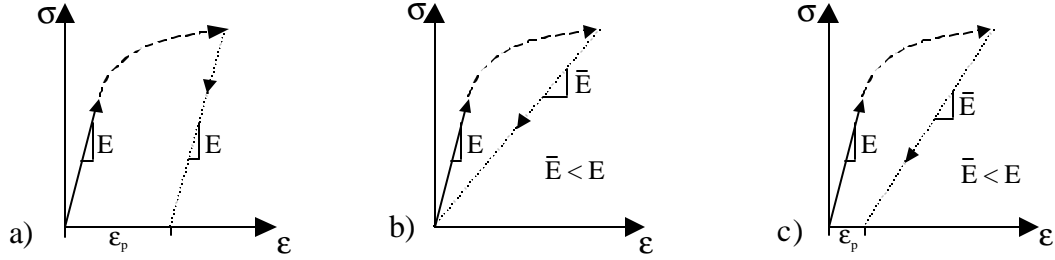
Figure 1. Idealized nonlinear material behavior. (a) Nonlinearity caused by *plasticity*, (b) Nonlinearity caused by *damage*, and (c) Nonlinearity caused by *plasticity* and *damage*.

3.1 Damage Tensor

   Within the context of continuum damage mechanics, distributed microscopic damage can be quantified by the use of an appropriate tensor field that describes the orientation and density of microcracks in the material. This damage tensor serves as an evolving internal variable within the framework of irreversible thermodynamics, and the local value of the damage tensor is used to define the damaged (i.e. reduced) stiffness of the material. Various forms of the damage tensor that have been proposed in the literature include scalars, vectors, 2nd order tensors, and 4th order tensors (Skrzypek and Ganczarski, 1999; Lemaitre, 1996). For the sake of computational efficiency, one should choose the simplest tensorial form that is capable of accurately describing the distribution, density, and orientation of microcracks and microvoids for the intended type of problem. For problems that can be idealized as beams, plates or shells, distributed damage can be described to an acceptable level of accuracy by a symmetric 2nd order tensor **D** whose principal directions are assumed to coincide with the principal material directions, i.e. orthotropic damage (Barbero and DeVivo, 2001). In the event that a particular material happens to be isotropic in its undamaged state, the principal material directions are simply chosen to coincide with the global coordinate system directions, i.e., two orthogonal in-plane directions and the transverse direction. The eigenvalues of the orthotropic damage tensor **D** (denoted D_1, D_2, and D_3) have a simple physical interpretation, namely, the ith eigenvalue D_i represents the effective fractional reduction in load carrying area on planes that are perpendicular to the ith principal material direction. These damage eigenvalues are illustrated in Figure 2 for the special case of a fiber reinforced composite material where the first principal material direction is chosen to coincide with the fiber direction.

   The eigenvalues of the damage tensor must be in the range $0 \leq D_i \leq 1$ where $D_i = 0$ corresponds to a complete lack of microcracks that are normal to the ith principal material direction, while $D_i = 1$ corresponds to a complete separation of the material across planes that are normal to the ith principal material direction.
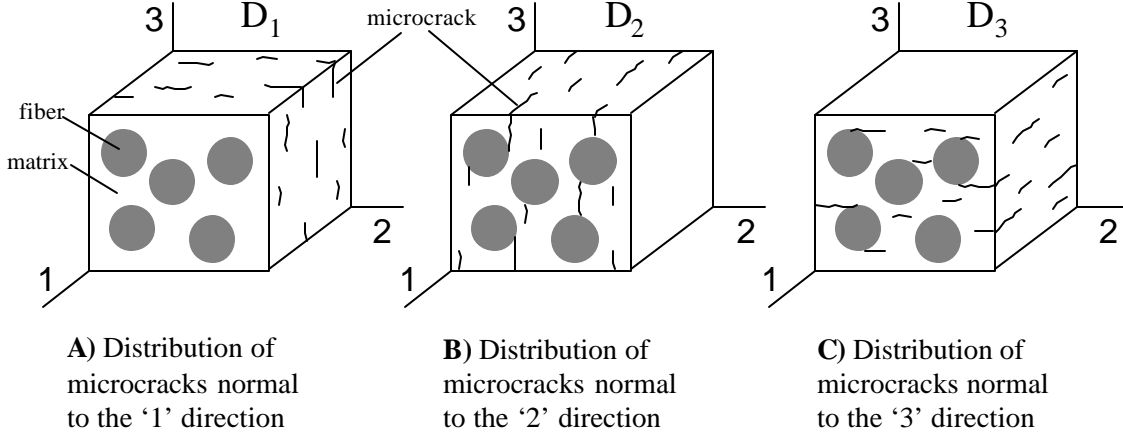
A) Distribution of microcracks normal to the '1' direction

B) Distribution of microcracks normal to the '2' direction

C) Distribution of microcracks normal to the '3' direction

Figure 2. Representative volume elements showing distribution of microcracks described by damage eigenvalues D_1, D_2 and D_3. D_i is interpreted as the effective fractional reduction in load carrying area due to microcracks that are normal to the ith principal material direction.

3.2 Damaged Constitutive Relations (Stiffness Reduction Scheme)

   In order to relate the damage eigenvalues to material stiffness reduction, we first define the concept of *effective* stress, denoted $\overline{\mathbf{S}}$, which represents an attempt to assign the actual internal material forces to cross sectional areas that have been reduced due to the presence of damage. Qualitatively speaking, we expect the effective stress $\overline{\mathbf{S}}$ to be greater than the apparent stress $\mathbf{S}$ (which uses the undamaged cross sectional area); however, the precise manner of defining the effective stress is somewhat arbitrary, and consequently numerous methods for defining effective stress have been proposed in the literature (Skrzypek and Ganczarski, 1999). In the present discussion, we use the symmetric effective stress tensor $\overline{\mathbf{S}}$ described by Cordebois and Sidoroff (1982) which can be expressed as

$$\overline{\mathbf{S}} \;=\; \left(\left(\sqrt{\mathbf{I}-\mathbf{D}} \right)^{-1} \cdot \mathbf{S} \cdot \left(\sqrt{\mathbf{I}-\mathbf{D}} \right)^{-\mathrm{T}} \right) \;=\; \mathbf{M}^{-1} : \mathbf{S} \tag{1}$$

where $\mathbf{M}$ is a 4th order symmetric tensor known as the *damage effects tensor*. When expressed in the principal material coordinate system using contracted notation, $\mathbf{M}$ can be represented by the following diagonal 6x6 matrix.

$$\begin{bmatrix} (1-D_1) & 0 & 0 & 0 & 0 & 0 \\ 0 & (1-D_2) & 0 & 0 & 0 & 0 \\ 0 & 0 & (1-D_3) & 0 & 0 & 0 \\ 0 & 0 & 0 & \sqrt{1-D_2}\sqrt{1-D_3} & 0 & 0 \\ 0 & 0 & 0 & 0 & \sqrt{1-D_3}\sqrt{1-D_1} & 0 \\ 0 & 0 & 0 & 0 & 0 & \sqrt{1-D_1}\sqrt{1-D_2} \end{bmatrix}$$

8

In this case, the effective stress components of Eq. (1) can now be expressed in the principal material coordinate system using contracted notation as follows.

$$\bar{s}_i = \frac{s_i}{(1-D_i)}, \quad \text{for i=1,2,3} \quad \text{(no summation implied)} \tag{1a}$$

$$\bar{s}_4 = \frac{s_4}{\sqrt{1-D_2}\sqrt{1-D_3}}, \quad \bar{s}_5 = \frac{s_5}{\sqrt{1-D_3}\sqrt{1-D_1}}, \quad \bar{s}_6 = \frac{s_6}{\sqrt{1-D_1}\sqrt{1-D_2}} \tag{1b,c,d}$$

Having adopted a definition for the effective stress tensor, we can now define the components of the *effective* strain tensor $\bar{\mathbf{e}}$ by insisting that the same elastic strain energy density should be obtained regardless whether it is computed with the apparent stress $\mathbf{s}$ and the apparent strain $\mathbf{e}$, or the effective stress $\bar{\mathbf{s}}$ and effective strain $\bar{\mathbf{e}}$. This is the so-called principle of equivalent elastic strain energy density, which can be expressed as $(1/2)\bar{\mathbf{s}}:\bar{\mathbf{e}} = (1/2)\mathbf{s}:\mathbf{e}$. Substitution of $\mathbf{M}:\bar{\mathbf{s}} = \mathbf{s}$ and noting that $\bar{\mathbf{s}}$, $\mathbf{e}$ and $\mathbf{M}$ are symmetric, yields $\bar{\mathbf{e}} = \mathbf{M}:\mathbf{e} = \mathbf{e}:\mathbf{M}$. In this case, the effective strain components can be expressed in the principal material coordinate system using contracted notation as follows.

$$\bar{e}_i = e_i(1-D_i), \quad \text{for i=1,2,3 (no summation implied)} \tag{3a}$$

$$\bar{e}_4 = e_4\sqrt{1-D_2}\sqrt{1-D_3}, \quad \bar{e}_5 = e_5\sqrt{1-D_3}\sqrt{1-D_1}, \quad \bar{e}_6 = e_6\sqrt{1-D_1}\sqrt{1-D_2} \tag{3b,c,d}$$

The presence of distributed microscopic damage, as defined by the internal variable **D,** affects the Helmholtz free energy density Ψ, which is postulated to be the sum of an elastic strain energy density φ and a free energy $\Pi(\beta)$ that is associated with damage hardening.

$$? \ = \ ?(\mathbf{e},\mathbf{D},b) = \frac{1}{r}j(\mathbf{e},\mathbf{D}) + ?(b) \tag{4}$$

In Eq. (4), the internal variable β is a non-dimensional damage hardening parameter that characterizes the overall state of damage and is used to control the process of damage hardening. Assuming that the homogenized composite material exhibits a linear elastic stress/strain relationship up to the point of damage initiation or up to the point of further damage progression, the elastic strain energy density can be expressed as $j(\mathbf{e},\mathbf{D}) = (1/2)\mathbf{s}:\mathbf{e} = (1/2)\mathbf{e}:\bar{\mathbf{C}}:\mathbf{e}$, where $\bar{\mathbf{C}} = \bar{\mathbf{C}}(\mathbf{D})$ is the 4th order *damaged* material elasticity tensor. The dependence of $\bar{\mathbf{C}}$ on the damage tensor **D** is defined by requiring that the elastic strain energy density of the *damaged* material that is subjected to the apparent strain **e** should be equivalent to the stain energy density of the *undamaged* material that is subjected to the effective (or reduced) strain $\bar{\mathbf{e}}$. Upon introducing the expression ($\bar{\mathbf{e}} = \mathbf{M}:\mathbf{e} = \mathbf{e}:\mathbf{M}$) into the strain energy equivalence principle, the damaged material elasticity tensor can be defined as $\bar{\mathbf{C}} = \mathbf{M}:\mathbf{C}:\mathbf{M}$. $\bar{\mathbf{C}}$ can be more simply expressed in the principal material coordinate system using contracted notation as a symmetric 6×6 matrix that is indicative of an *orthotropically damaged* material. In this

case, the nonzero components of $\overline{\mathbf{C}}$ are given by Eq. (5) where repeated indices do not imply summation.

$$\overline{C}_{ab} = C_{ab}(1-D_a)(1-D_b) \quad \text{for } \alpha,\beta=1,2,3 \tag{5a}$$

$$\overline{C}_{44}=C_{44}(1-D_2)(1-D_3), \quad \overline{C}_{55}=C_{55}(1-D_3)(1-D_1), \quad \overline{C}_{66}=C_{66}(1-D_1)(1-D_2) \tag{5b,c,d}$$

3.3 The damage surface and the damage evolution equations

After having defined stiffness reduction in terms of the damage eigenvalues, we must now develop the evolution equations for the damage eigenvalues. Increments in the free energy density $\rho\Psi$ can be expressed in terms of increments in the kinematic variables and internal variables ($\mathbf{e}, \mathbf{D}, \beta$) as

$$\Delta(r?) = \frac{\partial(r?)}{\partial\mathbf{e}}:\Delta\mathbf{e} + \frac{\partial(r?)}{\partial\mathbf{D}}:\Delta\mathbf{D} + \frac{\partial(r?)}{\partial b}\Delta b \tag{6}$$

where the partial derivatives in Eq. (6) define the generalized thermodynamic forces that are energy conjugate to the variables $\mathbf{e}, \mathbf{D}$ and β. Partial differentiation of $\rho\Psi$ with respect to the apparent strain tensor $\mathbf{e}$ defines the apparent Cauchy stress tensor $\mathbf{s}$ that acts on the damaged material.

$$\mathbf{s} = \frac{\partial(r?)}{\partial\mathbf{e}} = \frac{\partial j}{\partial\mathbf{e}} = \frac{\partial\left(\frac{1}{2}\mathbf{e}:\overline{\mathbf{C}}:\mathbf{e}\right)}{\partial\mathbf{e}} = \overline{\mathbf{C}}:\mathbf{e} \tag{7}$$

Partial differentiation of $\rho\Psi$ with respect to the damage tensor $\mathbf{D}$ yields a 2nd order, symmetric, negative semidefinite tensor $\mathbf{Y}$ that is energy conjugate to the damage tensor. However, it is common convention to include a sign change in the definition, i.e. $\mathbf{Y} \equiv -\partial(\rho\Psi)/\partial\mathbf{D}$, in which case $\mathbf{Y}$ is interpreted as the damage energy release rate tensor.

$$\mathbf{Y} = -\frac{\partial(r?)}{\partial\mathbf{D}} = -\frac{\partial j}{\partial\mathbf{D}} = -\frac{\partial\left(\frac{1}{2}\mathbf{e}:\overline{\mathbf{C}}:\mathbf{e}\right)}{\partial\mathbf{D}} = -\frac{1}{2}\mathbf{e}:\frac{\partial\overline{\mathbf{C}}}{\partial\mathbf{D}}:\mathbf{e} \tag{8}$$

Eq. (8) can be conveniently expressed in the principal material coordinate system via use of Eqs. (5), yielding the following expressions for the damage energy release rate eigenvalues.

$$Y_1 = C_{11}(1-D_1)e_1^2 + C_{12}(1-D_2)e_1e_2 + C_{13}(1-D_3)e_1e_3 + \frac{C_{55}}{2}(1-D_3)e_5^2 + \frac{C_{66}}{2}(1-D_2)e_6^2$$

$$Y_2 = C_{21}(1-D_1)e_1e_2 + C_{22}(1-D_2)e_2^2 + C_{23}(1-D_3)e_2e_3 + \frac{C_{44}}{2}(1-D_3)e_4^2 + \frac{C_{66}}{2}(1-D_1)e_6^2$$

$$Y_3 = C_{31}(1-D_1)e_1e_3 + C_{32}(1-D_2)e_3e_2 + C_{33}(1-D_3)e_3^2 + \frac{C_{44}}{2}(1-D_2)e_4^2 + \frac{C_{55}}{2}(1-D_1)e_5^2$$

$$\tag{9a,b,c}$$

Partial differentiation of $\rho\Psi$ with respect to the overall damage parameter β yields a generalized thermodynamic force referred to as the damage hardening variable $\gamma(\beta)$.

$$\boldsymbol{g} = \boldsymbol{g}(\boldsymbol{b}) = \frac{\partial(\boldsymbol{r}?\,)}{\partial \boldsymbol{b}} = \frac{\partial \Pi}{\partial \boldsymbol{b}} \tag{10}$$

A linear relationship $\gamma = c_1\beta$ is often used for damage hardening (Voyiadjis and Kattan, 1999; Lee et al., 1985); however, an exponential form such as $\boldsymbol{g} = c_1\left(1 - e^{b/c_2}\right)$ is often better able to represent the damage hardening characteristics observed in fiber-reinforced composites (Barbero and DeVivo, 2001).

It is postulated that *damaging behavior* can be distinguished from *non-damaging behavior* on a local basis by a convex damage surface $g(\mathbf{Y},\gamma) = 0$ that is defined in energy release rate space, where $g(\mathbf{Y},\gamma) < 0$ indicates a non-damaging state, $g(\mathbf{Y},\gamma) = 0$ indicates a damage inducing state, and $g(\mathbf{Y},\gamma) > 0$ is understood to be inadmissible. The damage surface is often assumed to be a quadratic function of the energy release rate tensor[18,20,23]. As a specific example, we consider the following damage surface, expressed in the principal material coordinate system.

$$g(\mathbf{Y},\boldsymbol{g}) = \sqrt{J_{11}Y_{\mathbf{1}}^2 + J_{22}Y_{\mathbf{2}}^2 + J_{33}Y_{\mathbf{3}}^2} - (\boldsymbol{g}_0 + \boldsymbol{g}(\boldsymbol{b})) \tag{11}$$

In Eq. (11), J_{11}, J_{22}, and J_{33} represent experimentally derived material constants that define the damage tolerance of the material, and effectively control the shape of the damage surface. The expression $\gamma_0 + \gamma(\beta)$ defines the current damage threshold and thus controls the size of the damage surface. The material constant γ_0 defines the initial damage threshold of the un-damaged material, and $\gamma(\beta)$ provides the increase in the damage threshold (i.e. damage hardening) that occurs as the damage tensor $\mathbf{D}$ evolves. Note that the energy release rate eigenvalues, as defined in Eqs. (9), are positive semidefinite quantities, regardless whether the material exhibits tensile deformation or compressive deformation. Thus the simple damage surface defined by Eq. (11) is unable to account for materials that are more easily damaged in tension than compression. For a discussion of models that incorporate this unilateral effect, the reader is referred to Ladeveze (2002) and Dragon (2002).

The damage surface of Eq. (11) defines the limits of non-damaging behavior at an arbitrary point in the material. As long as the material exhibits variables (Y_1, Y_2, Y_3, γ) that identify points interior to the current damage surface $g(\mathbf{Y},\gamma) = 0$, then no further damage occurs at the local material point where Y_1, Y_2, Y_3, and γ are measured. However, when these variables cause the damage surface $g(\mathbf{Y},\gamma)$ to be reached or exceeded, then damage is assumed to progress in a manner that is consistent with the Kuhn-Tucker conditions ($g \leq 0$, $d\gamma \geq 0$, and $g \cdot d\gamma = 0$) which imply that the condition $g=0$ (or alternately $dg = 0$) must be maintained during a damaging process. In other words, any attempt to reach a point $(\mathbf{Y},\gamma)$ that would cause $g(\mathbf{Y},\gamma) > 0$ results in a simultaneous increase in the damage tensor $\mathbf{D}$ and the damage hardening variable γ in such a way as to maintain the condition $g(\mathbf{Y},\gamma) = 0$ throughout the damaging process.

The exact manner in which the internal variables **D** and γ evolve is provided by the Principle of Maximum Dissipation which states that during a damaging (i.e. dissipative) process, the actual values of the thermodynamic forces **Y** and γ will cause the dissipation power density Φ to be extremized, subject to the constraint that g=0 (Lee et al., 1985). For the case of *elastic* damage (i.e. damage without accompanying plasticity), the dissipation power density can be expressed in the principal material coordinate system as

$$\Phi(\mathbf{Y}, \boldsymbol{g}) = Y_I \dot{D}_I - \boldsymbol{g}\dot{\boldsymbol{b}} \geq 0 \tag{12}$$

In order to extremize the dissipation power density subject to the constraint g(**Y**,γ)=0, we introduce the Lagrange multiplier λ and form the modified objective function Φ^*.

$$\Phi^*(\mathbf{Y}, \boldsymbol{g}) = Y_I \dot{D}_I - \boldsymbol{g}\dot{\boldsymbol{b}} - \boldsymbol{l}g \tag{13}$$

Extremization of Φ^* with respect to the variables **Y** and γ yields

$$\frac{\partial \Phi^*}{\partial Y_I} = \dot{D}_I - \boldsymbol{l}\frac{\partial g}{\partial Y_I} = 0 \quad \rightarrow \quad \dot{D}_I = \boldsymbol{l}\frac{\partial g}{\partial Y_I} \tag{14a}$$

$$\frac{\partial \Phi^*}{\partial \boldsymbol{g}} = -\dot{\boldsymbol{b}} - \boldsymbol{l}\frac{\partial g}{\partial \boldsymbol{g}} = 0 \quad \rightarrow \quad \dot{\boldsymbol{b}} = -\boldsymbol{l}\frac{\partial g}{\partial \boldsymbol{g}} \tag{14b}$$

Eqs. (14) express the rate of change of the damage tensor components and the overall damage parameter in terms of the common Lagrange multiplier λ. The value of λ can be determined from the consistency condition which requires that during a damaging process, the damage surface should evolve in such a way that g=0 (or alternately $\dot{g}=0$) is maintained.

$$\dot{g}(\mathbf{Y}, \boldsymbol{g}) = \frac{\partial g}{\partial Y_I}\dot{Y}_I + \frac{\partial g}{\partial \boldsymbol{g}}\dot{\boldsymbol{g}} = 0 \tag{15}$$

Eqs. (14) and (15) provide the relationships that are needed to determine the evolution of the damage tensor **D** and the overall damage parameter β. The Lagrange multiplier ? can be eliminated from this system of equations to yield

$$\dot{D}_I = \left(\frac{\dfrac{\partial g}{\partial Y_K}\dot{Y}_K}{\dfrac{\partial g}{\partial \boldsymbol{g}}\dfrac{\partial \boldsymbol{g}}{\partial \boldsymbol{b}}\dfrac{\partial g}{\partial \boldsymbol{g}}} \right)\frac{\partial g}{\partial Y_I} = \left(\frac{\dfrac{\partial g}{\partial Y_I}\dfrac{\partial g}{\partial Y_K}}{\dfrac{\partial g}{\partial \boldsymbol{g}}\dfrac{\partial \boldsymbol{g}}{\partial \boldsymbol{b}}\dfrac{\partial g}{\partial \boldsymbol{g}}} \right)\dot{Y}_K = Z_{IK}\dot{Y}_K \tag{16a}$$

$$\boldsymbol{\dot{b}} = -\left(\frac{\dfrac{\partial g}{\partial Y_K}\dot{Y}_K}{\dfrac{\partial g}{\partial \boldsymbol{g}}\dfrac{\partial \boldsymbol{g}}{\partial \boldsymbol{b}}\dfrac{\partial g}{\partial \boldsymbol{g}}}\right)\frac{\partial g}{\partial \boldsymbol{g}} = -\left(\frac{\dfrac{\partial g}{\partial Y_K}}{\dfrac{\partial g}{\partial \boldsymbol{g}}\dfrac{\partial \boldsymbol{g}}{\partial \boldsymbol{b}}}\right)\dot{Y}_K = W_K\dot{Y}_K \tag{16b}$$

where the quantities Z_{IK} and W_K have been introduced for convenience. The time variable can be eliminated from Eq. (16) to yield an expression which relates increments in the damage eigenvalues and overall damage parameter to increments in the energy release rate eigenvalue.

$$dD_I = Z_{IK}\,dY_K, \qquad d\beta = W_K\,dY_K \tag{17a,b}$$

In its present form, Eq. (17) is not particularly useful since it is not practical to *impose* increments in the energy release rate eigenvalues. However, Eq. (17) can be converted to an *imposed strain* form by invoking Eq. (9) [$\mathbf{Y} = \mathbf{Y}(\mathbf{e},\mathbf{D})$] to express dY_K as

$$dY_K = \frac{\partial Y_K}{\partial D_Q}dD_Q + \frac{\partial Y_K}{\partial e_a}de_a \tag{18}$$

where we have adopted contracted notation for the strain tensor components (i.e. $\varepsilon_1 \equiv \varepsilon_{11}$, $\varepsilon_2 \equiv \varepsilon_{22}$, $\varepsilon_3 \equiv \varepsilon_{33}$, $\varepsilon_4 \equiv 2\varepsilon_{23}$, $\varepsilon_5 \equiv 2\varepsilon_{31}$, $\varepsilon_6 \equiv 2\varepsilon_{12}$). Substitution of Eq. (18) into Eq. (17) permits the governing differential equations of damage evolution to be written in terms of $d\mathbf{D}$, $d\beta$ and $d\mathbf{e}$.

$$dD_I = Z_{IK}\frac{\partial Y_K}{\partial D_Q}dD_Q + Z_{IK}\frac{\partial Y_K}{\partial e_a}de_a \tag{19a}$$

$$d\boldsymbol{b} = W_K\frac{\partial Y_K}{\partial D_Q}dD_Q + W_K\frac{\partial Y_K}{\partial e_a}de_a \tag{19b}$$

Equation (19) can be solved for $d\mathrm{D}_I$ (I=1,2,3) and $d\beta$, yielding the following *imposed strain* form of the damage evolution equations.

$$\begin{Bmatrix} dD_1 \\ dD_2 \\ dD_3 \\ d\boldsymbol{b} \end{Bmatrix} = [\mathbf{T}]\{d\mathbf{e}\}. \tag{20}$$

In Eq. (20), the 4×6 matrix [$\mathbf{T}$] can be expressed as $[\mathbf{A}]^{-1}[\mathbf{B}]$, where the 4×4 matrix [$\mathbf{A}$] and the 4×6 matrix [$\mathbf{B}$] are defined as

$$[\mathbf{A}] = \begin{bmatrix} 1 - Z_{1K}\dfrac{\partial Y_K}{\partial D_1} & -Z_{1K}\dfrac{\partial Y_K}{\partial D_2} & -Z_{1K}\dfrac{\partial Y_K}{\partial D_3} & 0 \\[2ex] -Z_{2K}\dfrac{\partial Y_K}{\partial D_1} & 1 - Z_{2K}\dfrac{\partial Y_K}{\partial D_2} & -Z_{2K}\dfrac{\partial Y_K}{\partial D_3} & 0 \\[2ex] -Z_{2K}\dfrac{\partial Y_K}{\partial D_1} & -Z_{3K}\dfrac{\partial Y_K}{\partial D_2} & 1 - Z_{3K}\dfrac{\partial Y_K}{\partial D_3} & 0 \\[2ex] -W_K\dfrac{\partial Y_K}{\partial D_1} & -W_K\dfrac{\partial Y_K}{\partial D_2} & -W_K\dfrac{\partial Y_K}{\partial D_3} & 1 \end{bmatrix}, \tag{21a}$$

$$[\mathbf{B}] = \begin{bmatrix} Z_{1K}\dfrac{\partial Y_K}{\partial \boldsymbol{e}_1} & Z_{1K}\dfrac{\partial Y_K}{\partial \boldsymbol{e}_2} & Z_{1K}\dfrac{\partial Y_K}{\partial \boldsymbol{e}_3} & Z_{1K}\dfrac{\partial Y_K}{\partial \boldsymbol{e}_4} & Z_{1K}\dfrac{\partial Y_K}{\partial \boldsymbol{e}_5} & Z_{1K}\dfrac{\partial Y_K}{\partial \boldsymbol{e}_6} \\[2ex] Z_{2K}\dfrac{\partial Y_K}{\partial \boldsymbol{e}_1} & Z_{2K}\dfrac{\partial Y_K}{\partial \boldsymbol{e}_2} & Z_{2K}\dfrac{\partial Y_K}{\partial \boldsymbol{e}_3} & Z_{2K}\dfrac{\partial Y_K}{\partial \boldsymbol{e}_4} & Z_{2K}\dfrac{\partial Y_K}{\partial \boldsymbol{e}_5} & Z_{2K}\dfrac{\partial Y_K}{\partial \boldsymbol{e}_6} \\[2ex] Z_{3K}\dfrac{\partial Y_K}{\partial \boldsymbol{e}_1} & Z_{3K}\dfrac{\partial Y_K}{\partial \boldsymbol{e}_2} & Z_{3K}\dfrac{\partial Y_K}{\partial \boldsymbol{e}_3} & Z_{3K}\dfrac{\partial Y_K}{\partial \boldsymbol{e}_4} & Z_{3K}\dfrac{\partial Y_K}{\partial \boldsymbol{e}_5} & Z_{3K}\dfrac{\partial Y_K}{\partial \boldsymbol{e}_6} \\[2ex] W_K\dfrac{\partial Y_K}{\partial \boldsymbol{e}_1} & W_K\dfrac{\partial Y_K}{\partial \boldsymbol{e}_2} & W_K\dfrac{\partial Y_K}{\partial \boldsymbol{e}_3} & W_K\dfrac{\partial Y_K}{\partial \boldsymbol{e}_4} & W_K\dfrac{\partial Y_K}{\partial \boldsymbol{e}_5} & W_K\dfrac{\partial Y_K}{\partial \boldsymbol{e}_6} \end{bmatrix}. \tag{21b}$$

3.4 Example - Damaged Response of the Adhesive Material

To demonstrate the material response characteristics predicted by the 3-D continuum damage mechanics model, we consider the homogeneous deformation and loading of a brittle epoxy adhesive material that is typical of the adhesives used to bond actuators to structural substrates. In its un-damaged (virgin) state, the adhesive material is assumed to be isotopic, with modulus E = 6.8 GPa and Poisson's ratio ν = 0.3. The damage surface constants and the damage hardening constants for the adhesive material are assumed as $J_{11} = J_{22} = J_{33} = 1$, $\gamma(\beta) = 2.5(10^6)\beta$, and $\gamma(0) = 0$. Two different load cases are considered. The first load case involves imposing a homogeneous state of simple shear deformation in the 1-3 plane (i.e., $\varepsilon_5 > 0$, all other ε_α are zero). This particular mode of deformation contributes equally to the evolution of damage eigenvalues D_1 and D_3, thus resulting in the accumulation of microcracks that are oriented normal to the '1' and '3' directions respectively. Part A of Figure 3 shows the non-linear softening stress/strain relationship predicted by the damage model. Note that the maximum value of shear stress attained in this displacement-controlled test is approximately 36 MPa. For a similar load-controlled shear test, the adhesive material simply exhibits complete material failure during any attempt to increase the imposed shear stress beyond 36 MPa. Part B of Figure 3 shows the evolution of damage eigenvalues D_1 and D_3 caused by the imposed shear deformation. Examination of Parts A and B reveals that when the maximum shear stress is attained, the magnitude of the damage eigenvalues D_1 and D_3 is approximately 0.24.
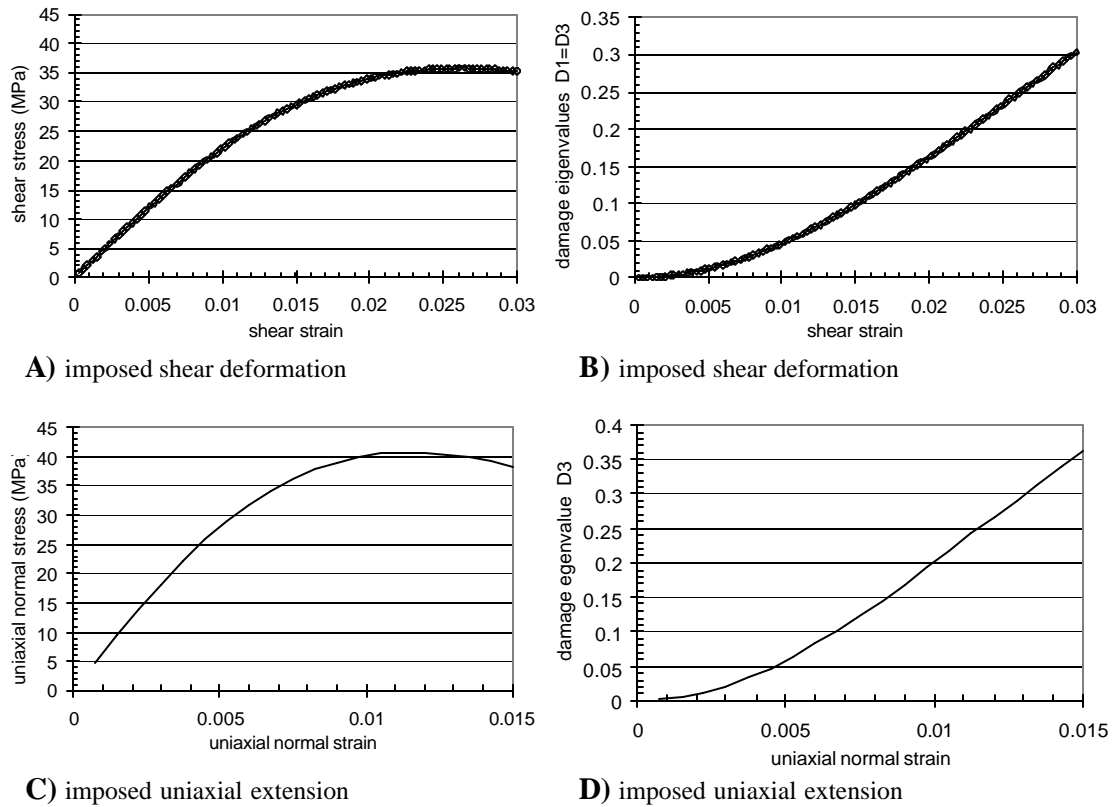
Next, consider the case where the adhesive material is subjected to uniaxial extension in the '3' direction. During the imposed extension, the material is free to undergo lateral contraction in the 1 and 2 directions so that it maintains a uniaxial stress state. This

14

particular mode of deformation contributes only to damage eigenvalue D_3, resulting in the accumulation of microcracks that are oriented normal to the '3' direction. Part C of Figure 3 shows the damaged uniaxial stress/strain relationship predicted by the damage model. Note that the maximum value of uniaxial normal stress that can be supported by the adhesive material is approximately 41 MPa; any attempt to load the adhesive material beyond this value results in complete failure of the material. Part D of Figure 3 shows the evolution of damage eigenvalue D_3 caused by the imposed axial extension. Examination of Parts C and D reveals that when the maximum uniaxial stress is attained, the magnitude of the damage eigenvalue D_3 is approximately 0.24.

A) imposed shear deformation

B) imposed shear deformation

C) imposed uniaxial extension

D) imposed uniaxial extension

Figure 3. Progressive damage in an adhesive material under homogeneous deformation and loading. A) Damaged stress/strain curve during imposed simple shear deformation in the 1-3 plane, B) Damage evolution during imposed simple shear deformation in the 1-3 plane, C) Damaged stress/strain curve during imposed uniaxial extension in the 3 direction, D) Damage evolution during imposed uniaxial extension in the 3 direction.

In Section 5, this particular adhesive material description is used in modeling the progressive adhesive damage that occurs in a simply-supported actuated plate subjected to bending actuation and distributed transverse loading.

4. Hierarchical, variable-kinematic, finite element model

To facilitate the goals of the present study, a 2-D, hierarchical, displacement-based, variable-kinematic finite element model is used for all simulations that are performed. The main attribute of the variable-kinematic finite element model that makes it suitable for the present study is that the kinematics and constitutive relations of any given element can be conveniently changed, thus allowing any given element to represent a wide variety of different laminate models ranging from the very simple to the very complex. In addition, the variable-kinematic finite element model permits different types of laminate elements (representing different types of laminate models) to be conveniently connected together in the same computational domain, thus permitting different subregions to be described by different mathematical models.

Within the context of the present study, the 2-D, hierarchical, displacement-based, variable-kinematic finite element is developed by expressing the total displacement field as the sum of a low order primary displacement field and a higher order secondary displacement field. The primary displacement field is present in all variable-kinematic elements at all times. The individual terms of the secondary displacement field then serve as relative displacements that can be added to the element's primary field to provide higher order kinematics as needed. The total displacement field is expressed as

$$u_\alpha(x,y,z) = u_\alpha^{FSD}(x,y,z) + u_\alpha^{LW}(x,y,z), \quad \alpha = 1,2,3 \tag{22}$$

where u_1, u_2, and u_3 are the total displacement components in the x, y, and z directions respectively. The primary displacement field is provided by $u_\alpha^{FSD}(x,y,z)$ which represents the assumed displacement field for the first order shear deformation theory (FSD) and is expressed as

$$u_1^{FSD}(x,y,z) = u_0(x,y) + z\theta_x(x,y), \tag{23a}$$
$$u_2^{FSD}(x,y,z) = v_0(x,y) + z\theta_y(x,y), \tag{23b}$$
$$u_3^{FSD}(x,y,z) = w_0(x,y). \tag{23c}$$

In Eqs. (23), $u_0(x,y)$, $v_0(x,y)$ and $w_0(x,y)$ represent the displacement of points on the plate's reference surface which is normally chosen to coincide with the plate's mid-surface. The terms $\theta_x(x,y)$ and $\theta_y(x,y)$ represent the rotation of the inextensible transverse normal fiber in the xz and yz planes respectively. The independent rotations $\theta_x(x,y)$ and $\theta_y(x,y)$ are not required to be equal in magnitude to the slopes dw_0/dx and dw_0/dy, thus the FSD displacement field includes a rudimentary transverse shear strain that is constant through the thickness of the laminate. Since the FSD displacement field does not explicitly include transverse normal strain, it is intended to be used in conjunction with a reduced constitutive matrix that is based on the assumption of zero transverse normal stress.

The secondary displacement field in Eq. (22), labeled as $u_\alpha^{LW}(x,y,z)$, represents the assumed displacement field for a full 3-D layerwise theory[28-30] which is characterized by displacement components that are piecewise continuous (specifically, C^0 continuous) with respect to the thickness coordinate. The layerwise displacement field is included as an optional, incremental enhancement to the primary displacement field, $u_\alpha^{FSD}(x,y,z)$, so that the element may have full or partial 3-D modeling capability when needed. Depending on

the desired level of accuracy, the variable-kinematic element can use none, part, or all of the layerwise field $u_\alpha^{LW}(x,y,z)$ to create a series of different elements having a wide range of kinematic complexity. For example, discrete layer transverse shear effects can be added to the element by including $u_1^{LW}(x,y,z)$ and $u_2^{LW}(x,y,z)$. Discrete layer transverse normal effects can be added to the element by including $u_3^{LW}(x,y,z)$. The layerwise field can be expressed as

$$u_1^{LW}(x,y,z) = U_j(x,y)\varphi_j(z) \tag{24a}$$
$$u_2^{LW}(x,y,z) = V_j(x,y)\varphi_j(z) \tag{24b}$$
$$u_3^{LW}(x,y,z) = W_j(x,y)\varphi_j(z) \tag{24c}$$

where the repeated subscript j implies summation over j=1,2,...,n. The functions $\varphi_j(z)$ (j=1,2,..,n) are 1-D Lagrangian interpolation functions associated with n nodes distributed through the laminate thickness, located at z_j (j=1,2,..,n). Thus the through-the-thickness variation of the displacement components is defined in terms of a 1-D finite element representation with C^0 continuity of the interpolants. The 1-D interpolants $U_j(x,y)$, $V_j(x,y)$, and $W_j(x,y)$ represent additions to the displacement components u_1, u_2, and u_3 on the planes defined by $z=z_j$ (j=1,2,..,n).   It should be noted that the layerwise field given by Eqs. (24) is sufficiently general to model any of the deformation modes that can be modeled by the FSD field given in Eqs. (23); thus, for elements that use all the variables shown in Eqs. (23) and (24), there will be five redundant variables that must be set to zero (or ignored) to permit a unique solution for the remaining variables. The presence of the FSD variables is essential for connecting different types of elements, thus five of the layerwise variables should be set to zero (for example, $U_1=U_n=0$, $V_1=V_n=0$, $W_1=0$).

A hierarchy of three distinctly different types of laminate elements can be obtained from the composite displacement field of Eq. (22), where the individual displacement expansions are defined by Eqs. (23) and (24). The first and simplest type of element is the first order shear deformation element (or FSD element). This element is formed using Eqs. (23) while ignoring Eqs. (24). The FSD element uses a reduced constitutive matrix that is derived based on the assumption of zero transverse normal stress.   The second type of element is the Type-I layerwise element (or LW1 element). The LW1 element is formed using Eqs. (23), (24a) and (24b), while ignoring (24c), thus the LW1 element includes discrete layer transverse shear effects but neglects transverse normal effects and consequently uses a reduced stiffness matrix similar to the FSD element. Due to the inclusion of discrete layer transverse shear effects, the LW1 element is applicable to thick laminates and often yields results comparable to 3-D finite elements while using approximately two thirds the number of degrees of freedom. The third and most complex element is the Type-II layerwise element (or LW2 element). The LW2 element is formed using both Eqs. (23) and (24), thus it is a full 3-D layerwise element that explicitly accounts for all six strain components, and consequently uses a full 3-D constitutive matrix.   The inclusion of the full layerwise field provides the LW2 element with both discrete layer transverse shear effects and discrete layer transverse normal effects. In terms of interpolation capability and number of degrees of freedom, the 2-D LW2 element is equivalent to an entire stack of conventional 3-D finite elements.

Since the first order shear deformation field is present in each of these three different types of elements, displacement continuity can be maintained throughout the mesh, even if

all three element types are simultaneously present in different parts of the mesh. This is achieved by simply enforcing homogeneous boundary conditions on some or all of the incremental layerwise variables along the boundaries that separate incompatible subregions, a process that is easily automated. A significant advantage afforded by the hierarchical formulation is that once the in-plane mesh is defined, the user can then assign any of the three element types (FSD, LW1, LW2) to any of the elements in the 2-D mesh. Subsequent changes in the type of any single element or group of elements can be performed with minimal effort, thus facilitating the goals of the present study.

4.1   Implementation of 3-D damage mechanics into the multilayer VKFE element

The 3-D continuum damage mechanics formulation described in Section 3 introduces two internal variables (the damage tensor **D** and the overall damage parameter β) whose evolution equations (Eq. 20) are developed within the framework of irreversible thermodynamics. In order to efficiently apply the damage formulation to fiber-reinforced laminated composite materials, several simplifying assumptions were invoked. First, the damage evolutions are applied to the homogenized description of the composite material instead of being separately applied to each of its constituent materials. Second, the homogenized composite material is assumed to exhibit orthotropic damage, hence the state of damage can be described by the three eigenvalues of a symmetric second order damage tensor ($\mathbf{D} \rightarrow D_1, D_2, D_3$). Third, the homogenized composite material is assumed to exhibit isotropic damage hardening which can be described by a scalar function of the overall damaged state.

The numerical implementation of this damage model in a first order shear deformable element was discussed by Robbins et al.[27] and is briefly summarized as follows. First, the polynomial order of the 2-D elements is restricted to linear or quadratic forms. Linear 2-D elements permit a better representation of damage localization, while quadratic elements offer superior performance in bending dominated problems. Second, the damage evolution equations are solved only at the discrete damage sampling points that are chosen to coincide with the reduced Gaussian integration points of the 2-D element. Third, based on the damage eigenvalues computed at the damage sampling points, the damage eigenvalues are interpolated over the 2-D element's reference surface using polynomials that are one order less than the displacement field. Fourth, integration in the thickness direction is performed using full quadrature; three Gauss points per material layer provides exact thickness integration of all terms even if the damage eigenvalues exhibit quadratic or cubic variation through the thickness of each material layer. Finally, the 2-D FSD element uses a *reduced* constitutive matrix that is stored as a full 6x6 matrix where the transverse normal components (row 3 and column 3) are set to zero; therefore, the 2-D FSD element can directly utilize the full 3-D damage mechanics equations in unaltered form. These implementation guidelines are also directly applicable to layerwise elements that use either linear or quadratic layers, and are used in the present study for all three element types (FSD, LW1 and LW2) that are derivable from the hierarchical VKFE finite element model.

5.   Numerical Results

In this section, the 3-D progressive damage model is used in conjunction with the 2-D, hierarchical, displacement-based, variable-kinematic finite element model to simulate damage accumulation in the adhesive bond layers of a simply-supported, actuated plate that is subjected to bending actuation and/or distributed transverse loading. Since the prediction of local damage evolution requires the use of a macroscopic model that is capable of delivering accurate 3-D stress and strain distributions within each constituent material of the actuated plate, the use of a first order shear deformation (FSD) model is not appropriate for the task; consequently, all simulations are performed using layerwise finite elements. It should be emphasized that the objective of this problem is not necessarily to produce a solution that agrees very closely with experimental results, but rather to demonstrate that the present methodology is adequate for such simulations and to investigate the fundamental characteristics of localized adhesive bond damage and its impact on the overall functionality of the actuated plate. In order to differentiate the relative contributions to local adhesive damage from transverse shear deformation and transverse normal deformation, both the LW1 and LW2 layerwise models are used to obtain solutions.

Figure 4 shows the geometry and boundary conditions of the simply-supported actuated plate that is used throughout the present study. The test specimen is composed of a square aluminum plate and a symmetric pair of square piezoceramic actuators that are bonded to the upper and lower surfaces of the aluminum plate via a thin adhesive layer. The relevant elastic and piezoelastic material properties that are assumed for the aluminum substrate, the piezoceramic actuator and the adhesive are listed below. Note that the stiffness of the adhesive material is one-tenth the stiffness of the piezoceramic actuator.

Elastic and piezoelectric constants for the un-damaged isotropic materials:
Aluminum: $E = 70$ GPa, $\nu = 0.3$,
Adhesive: $E = 6.3$ GPa, $\nu = 0.3$,
Piezoceramic: $E = 63$ GPa, $\nu = 0.3$, $d_{31} = d_{32} = -3.74537(10^{-7})$ mm/volt.

The length of the aluminum plate (2L) is fixed at twice the length of the piezoceramic actuators (2P). The thickness of each piezoceramic actuator is denoted as h. The thickness of the aluminum substrate is denoted as h_P, and the thickness of the adhesive layer is denoted as h_a. The total thickness of the actuated region is then $H=2h+2h_a+h_P$. While the total thickness H of the actuated region is varied in the study, the ratio of actuator thickness to aluminum thickness is fixed at $h/h_s=0.25$, and the ratio of adhesive thickness to actuator thickness is fixed at $h_a/h=0.10$. The edges of the aluminum plate at $x=\pm L$ and $y=\pm L$ are simply supported. Due to symmetries that exist along the x and y axes, the 2-D computational domain is reduced to one quadrant of the actuated plate. Parts B and C of Figure 4 show two different thickness configurations that are considered in the present study, namely, a relatively thick configuration characterized by an actuated span-to-thickness ratio 2P/H=2 and an aluminum plate span-to-thickness ratio $2L/h_P=6$, and a more moderate thickness configuration characterized by an actuated span-to-thickness ratio 2P/H=8 and an aluminum plate span-to-thickness ratio $2L/h_P=24$.

Two forms of loading are considered for the simply-supported actuated plate. The first form of loading consists of applying opposite electric fields to the top and bottom actuators, thus inducing global bending of the actuated plate. The second form of loading consists of applying a uniform distributed transverse load to the entire upper or lower surface of the actuated plate.

2-D computational domain ($0<X<L$, $0<Y<L$)
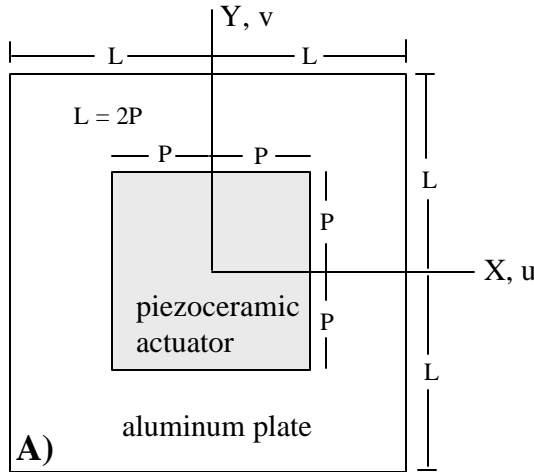
Simply Supported Boundary Conditions
At x=0: $u(0,y,z)=0$
At x=L: $v(L,y,z)=0$, $w(L,y,z)=0$
At y=0: $v(x,0,z)=0$
At y=L: $u(x,L,z)=0$, $w(x,L,z)=0$

piezoceramic actuator thickness h

adhesive bond thickness h_a

aluminum plate thickness h_P

total thickness of actuated region H

$h = 0.25 h_P$ $\qquad h_a = 0.10h$
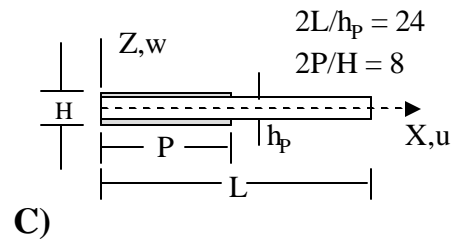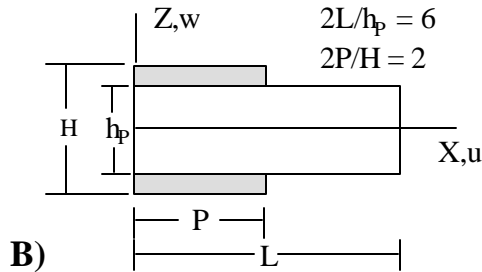
Figure 4. A) View of specimen geometry in XY plane and simply supported boundary conditions, B) Thickness configuration characterized by 2P/H=2 and 2L/h$_P$=6, C) Thickness configuration characterized by 2P/H=8 and 2L/h$_P$=24.

5.1 Effect of mesh density and model type on local adhesive layer deformation

Since local damage initiation and local damage progression are dependent on the local state of deformation, it is first necessary to determine the effects of 2-D mesh density and mathematical model type on the predicted local deformation in the adhesive bond layer. To this end, the simply-supported actuated plate is subjected to bending actuation without any distributed transverse loading, and linear elastic (non damaging) solutions are computed using the LW1 and LW2 layerwise models in conjunction with five different levels of 2-D mesh density. All five 2-D meshes are composed of 8-node, quadratic quadrilateral elements. Three of the 2-D meshes are uniform, while the remaining two meshes are nonuniform (i.e. graded) where the element size decreases as the two free edges of the actuator are approached. The three uniform 2-D meshes include a 6x6 uniform mesh, a 12x12 uniform mesh, and a 16x16 uniform mesh, denoted

20

respectively as 6x6u, 12x12u and 16x16u. Since the actuated region occupies one quadrant of the computational domain, the actuated region within the 6x6u, 12x12u and 16x16u meshes is discretized by uniform groups of 3x3 elements, 6x6 elements and 8x8 elements respectively. The two graded meshes include a 12x12 mesh (denoted 12x12g) where the smallest element at the actuator free edge has a width of P/40, and a 16x16 mesh (denoted 16x16g) where the smallest element (at the actuator edge) has a width of P/80. These two graded meshes are created in an attempt to provide increased resolution at the actuator free edge without increasing the problem size beyond that represented in the uniform meshes 12x12u and 16x16u.

It should be emphasized that certain types of physical phenomena such as damage, plasticity and wave propagation are often observed to exhibit non-smooth distributions with a high degree of localization. For problems involving these types of phenomena, the use of low order finite elements (particularly linear elements) is generally favored in practice since they minimize the domain over which a localized behavior is dispersed. However, in the modeling of structural members that exhibit significant bending behavior (e.g. beams, plates, shells), quadratic elements are known to be superior to linear elements since the latter exhibits a much higher degree of spurious transverse shear stiffness[27]. Therefore, despite the fact that quadratic elements are not as appropriate for modeling localized, non-smooth behavior as linear elements, the present study is conducted using quadratic elements due to their ability to deliver higher quality strain distributions for bending dominated problems.

Regardless of the layerwise model type or the level of 2-D mesh density, all solutions are computed using the same modest level of transverse discretization that consists of two equal linear layers for each of the piezoceramic actuators, one linear layer for each of the adhesive bond layers and four equal linear layers for the aluminum plate. Since the adhesive material is modeled with a single linear layer, the computed transverse shear strain and transverse normal strain in the adhesive layer necessarily represent the thickness average values of these quantities in the adhesive layer. This particular level of transverse discretization is chosen because it is coarse enough to be practical for larger problems, while still permitting a reasonably accurate, piecewise-constant representation of the transverse strains through the thickness of the three materials.

Figure 5 shows a representative selection of transverse shear strain and transverse normal strain distributions in the adhesive layer caused by imposing an actuation strain magnitude of $\varepsilon_1=\varepsilon_2=0.001$ in the piezoceramic patches. The transverse strains shown in Figure 5 are computed along a diagonal line that runs from the center of the actuator to the free corner of the actuator. This particular distribution is shown since the free corner of the adhesive layer exhibits the most severe local strain state. Representative linear elastic results are shown for both the LW1 and LW2 models using all five levels of 2-D mesh density; specifically, the transverse shear strain distribution is shown for the LW1 model, and the transverse normal strain distribution is shown for the LW2 model. In each case, the strain values are computed only at the reduced Gaussian integration points within each element and these computed values are marked by various symbols in parts A through D of Figure 5. Parts A and B of Figure 5 show results for the thicker actuated plate configuration (2P/H=2), while parts C and D show the results for the thinner actuated plate configuration (2P/H=8).
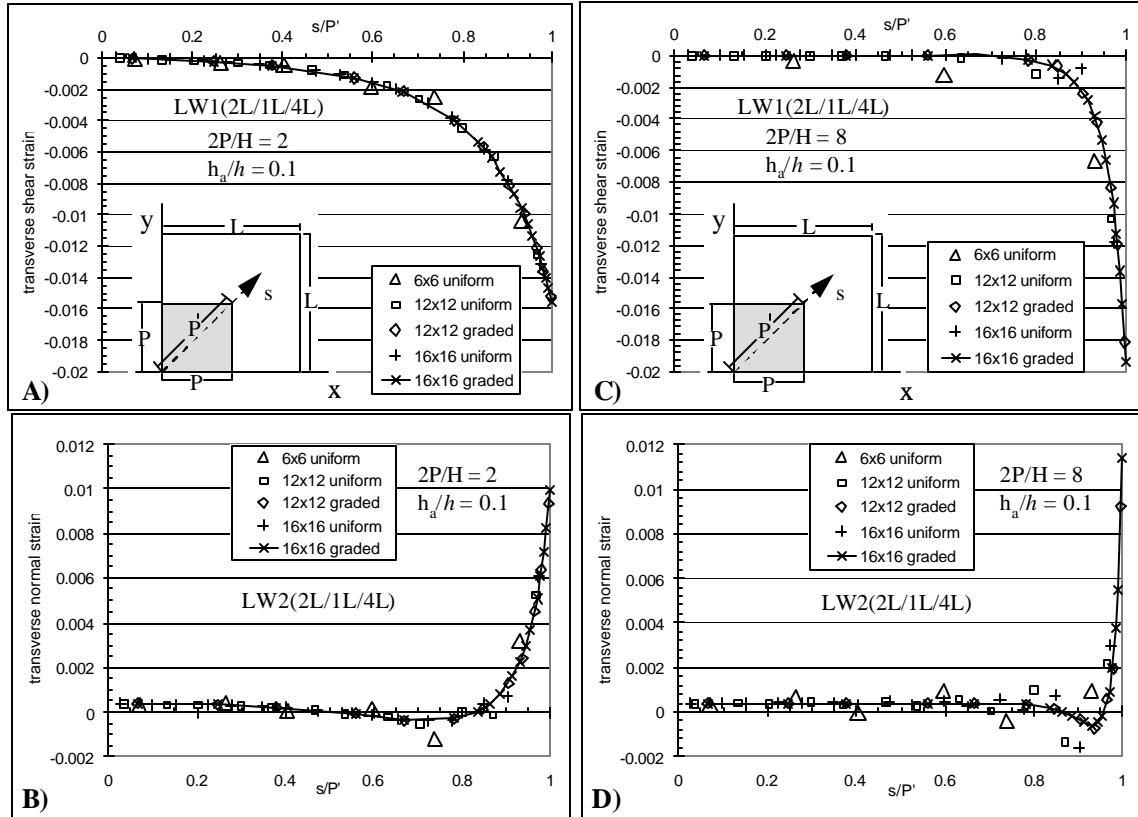
Figure 5. Comparison of adhesive strain distribution near the free corner of the upper actuator patch as predicted by linear elastic LW1 and LW2 models for the case of bending actuation of a simply supported plate.

As seen in parts A through D of Figure 5, all five levels of 2-D mesh density are capable of producing a local adhesive response with qualitatively correct characteristics. In each case, the transverse strains are insignificantly small in the interior region of the actuator and increase dramatically as the free corner of the actuator is approached. To aid visualization of the transverse strain distributions, the individual computed values of the most refined mesh (16x16g) are connected by straight lines. The main difference between the computed results from the two thickness configurations (2P/H=2 vs. 2P/H=8) is the width of the boundary layer region over which the transverse strains attain significant magnitude. For the thicker configuration (2P/H=2), the width of the adhesive boundary layer region is approximately 0.5P, while for the thinner configuration (2P/H=8), the width of the adhesive boundary layer region is approximately 0.15P.

For the thicker configuration (2P/H=2), the results from the 12x12u, 12x12g, 16x16u and 16x16g meshes show very good agreement with all computed strain values lying on a smooth curve, while the results from the 6x6u mesh can are seen to exhibit a mild oscillation about the smooth curve. For the thinner configuration (2P/H=8), the width of the boundary layer region is too narrow to be adequately resolved by either of the three uniform meshes (6x6u, 12x12u, 16x16u); however, the results from the two graded meshes (12x12g and 16x16g) show very good agreement with all computed values lying on a single smooth curve.

Based on the results shown in Figure 5, the 12x12g mesh is observed to offer the best compromise between solution quality and computational efficiency. It should be noted that the 16x16g mesh consistently produces peak transverse strains that are slightly higher than those produced by the 12x12g mesh; however, this difference is not anticipated to significantly affect the results of a progressive damage analysis, since it simply results in a slightly earlier initiation of local damage in the 16x16g mesh. Once local damage is initiated, the strain distributions no longer exhibit the sharp peaks as seen in Figure 5, thus the extra local resolution of the 16x16g mesh is not warranted given its increased computational cost.

Assuming then that the 12x12g mesh is adequate for providing the necessary resolution of the transverse strains in the adhesive boundary layer region, Figure 6 shows a comparison of the linear elastic stress distributions predicted by the LW1 and LW2 models on the 12x12g mesh. Examination of Figure 6 reveals that for both thickness configurations (2P/H=2 and 2P/H=8), the LW1 model and LW2 model predict similar transverse shear stress distributions in the adhesive layer, with the LW1 predicting slightly higher transverse shear stress than the LW2 model. However, the LW1 model is based on the assumption of zero transverse normal stress, while the LW2 model predicts that the peak transverse normal stress is approximately twice the magnitude of the peak transverse shear stress. Normally, neglecting the transverse normal stress is an accepted component of most beam, plate and shell models; however, in the remainder of this study, the explicit inclusion of transverse normal stress is shown to have a profound effect on local damage progression. Finally, the LW1 and LW2 models differ in the predicted local distribution of inplane normal stress within the boundary layer region, namely, the LW2 model shows a marked increase in inplane normal stress as the free corner of the actuator is approached, while the LW1 model shows very little change in inplane normal stress as the free corner of the actuator is approached
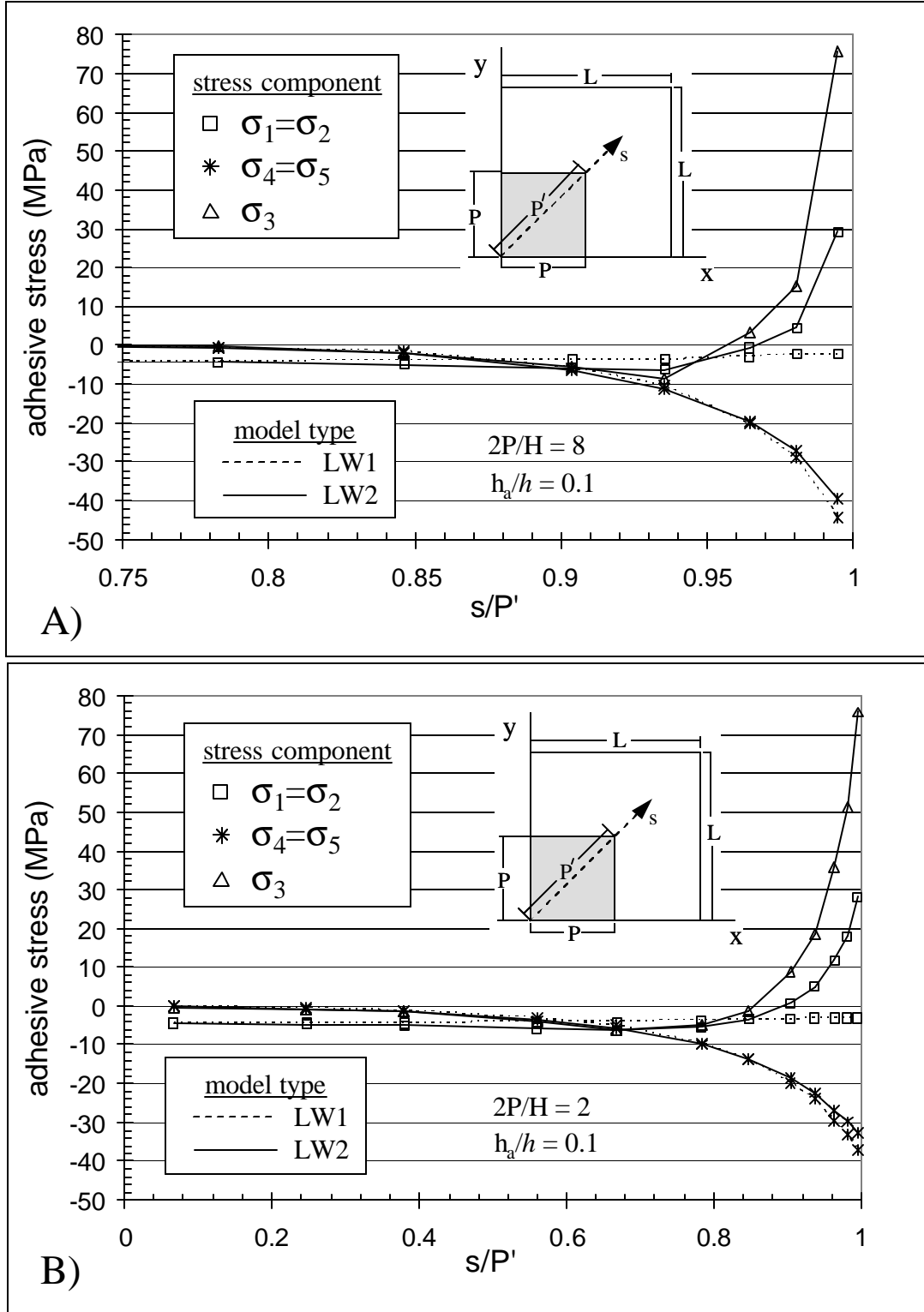
Figure 6. Comparison of adhesive stress distribution near the corner of the upper actuator patch as predicted by linear elastic LW1 and LW2 models for the case of bending actuation of a simply supported plate. Imposed actuation strain in the piezoceramic patch is $\varepsilon_1=\varepsilon_2=0.001$.

5.2 Progressive damage of the adhesive layer under imposed bending actuation

Now let us consider the local damage evolution that occurs in the adhesive layer of the simply-supported actuated plate when subjected to bending actuation alone, without any other form of mechanical loading. In this case, the top and bottom actuators are subjected to opposite voltages of equal magnitude causing the plate to bend. The objective is to determine the mode, severity and extent of damage in the adhesive bond layer as influenced by the choice of model type (LW1 vs. LW2) and the thickness configuration of the actuated plate. To this end, two different thickness configurations (2P/H=2 and 2P/H=8) are simulated using both LW1 and LW2 models. Based on the results of the previous section, the 12x12g 2-D mesh is utilized in each case. Furthermore, the present analyses make use of the same level of thickness discretization used in the previous section, namely, two equal linear layers for each of the piezoceramic actuators, one linear layer for each of the adhesive bond layers and four equal linear layers for the aluminum plate.

The aluminum material and piezoceramic material are modeled as linear elastic materials, while the adhesive material is permitted to exhibit progressive damage (material nonlinearity). The damage surface constants and the damage hardening constants that are assumed for the adhesive material are given below (same as used in Section 3.4).

Adhesive damage surface constants: $J_{11} = J_{22} = J_{33} = 1$,
Adhesive damage hardening: $\gamma(\beta) = 2.5(10^6)\beta$ and $\gamma(0) = 0$.

For both thickness configurations, the peak electric field applied to each actuator is sufficient to produce inplane normal strains of $\varepsilon_1 = \varepsilon_2 = 0.001$ in an unconstrained piezoceramic patch. This peak electric field is achieved by the application of a series of 20 equal load increments and is chosen because it represents the upper limit of actuation strain that can be obtained with a typical piezoceramic material.

For the maximum imposed actuation strain (0.001), Parts A through D of Figure 7 show the distribution of damage eigenvalues in the adhesive layer as predicted by the LW1 and LW2 models for both thickness configurations. Parts A and C show the adhesive damage eigenvalues D_1 and D_3 plotted along the x axis (normalized coordinate $0 < r/P < 1$) for the thickness configurations 2P/H=2 and 2P/H=8 respectively. Both the LW1 model and the LW2 model predict that significant levels of adhesive damage occur only within the boundary layer region with the maximum damage occurring at the free edge of the adhesive ($r/P = 1$). Furthermore, both models predict slightly higher damage for the thicker configuration (2P/H=2) than for the thinner configuration (2P/H=8), and both models predict peak local damage values of less than 0.10 along the x axis. However, the two models show some disagreement on the relative magnitudes of the damage eigenvalues. For example, the LW2 model predicts $D_3 > D_1$ while the LW1 model predicts $D_3 \approx D_1$. This can be explained by the fact that the LW1 model does not include transverse normal stress; therefore, local adhesive damage is primarily driven by the transverse shear stress σ_{xz} which contributes equally to D_1 and D_3 in the adhesive. In contrast, local adhesive damage in the LW2 model is driven by both transverse shear

stress σ_{xz} and transverse normal stress σ_{zz}. Since the transverse normal stress σ_{zz} contributes to D_3 but not to D_1, the LW2 model predicts that $D_3 > D_1$.

Parts B and D of Figure 7 show the adhesive damage eigenvalues D_1, D_2 and D_3 plotted along the free edge of the adhesive layer (normalized coordinate $0 < e/P < 1$) for the thickness configurations 2P/H=2 and 2P/H=8 respectively. Both the LW1 model and the LW2 model predict that adhesive damage is relatively constant over much of the free edge of the adhesive but then increases dramatically as the free corner of the adhesive is approached (i.e. as e/P→1). This increased damage near the free corner is caused by higher stress concentration that results from the two free edges that meet at a right angle. At the free corner of the adhesive, both the LW1 and LW2 models predict that D_3 is much larger than D_1 or D_2, thus the local damaged state clearly suggests the early stages of a local delamination (debonding), i.e., distributed microcracks that are oriented perpendicular to the transverse (z) direction . However, the value of D_3 predicted by the LW2 model is significantly higher than the value of D_3 predicted by the LW1 model. Again, the LW2 model's higher value of D_3 is caused by the fact that the LW2 model explicitly includes transverse normal stress which achieves a very high tensile value near the free edge and makes a significant contribution to the growth of D_3. Both models predict that $D_1 = D_2$ at the free corner (e/P=1) which can be understood by noting that the diagonal line x=y is an axis of symmetry which results in $\sigma_{xx} = \sigma_{yy}$ and $\sigma_{xz} = \sigma_{yz}$ at e/P=1. Thus the stress components that contribute to D_1 are equal to the stress components that contribute to D_2.
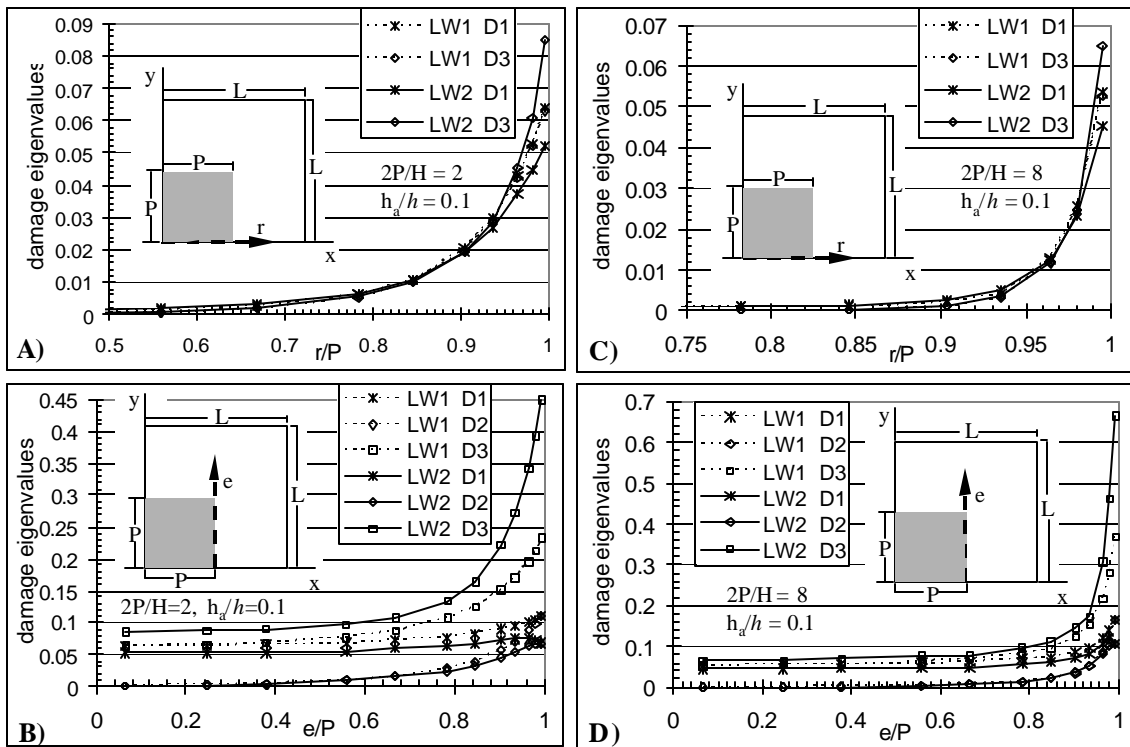

Figure 7. Comparison of damage distribution in the adhesive layer as predicted by LW1 and LW2 models for the case of bending actuation of a simply supported plate. Imposed actuation strain = 0.001.

Given the fact that the highest adhesive damage occurs at the free corner of the adhesive layer, Figures 7 through 9 show the predicted damage distributions and predicted stress distributions in the adhesive layer along a diagonal line that runs from the center of the actuated region to the free corner of the actuator (normalized coordinate $0 < s/P' < 1$). Parts A and B of Figure 8 show the distribution of damage eigenvalues in the thicker configuration ($2P/H=2$) at various levels of induced actuator strain, as predicted by both the LW1 and LW2 models. Examination of Figure 8 reveals several noteworthy trends. First, both models predict that damage is highest at the free corner of the adhesive layer (i.e. at $s/P'=1$) and becomes insignificant as the center of the actuator is approached (i.e., as $s/P' \rightarrow 0$). Second, both models predict that the damage eigenvalue D_3 is significantly higher than damage eigenvalues D_1 and D_2, thus the primary form of adhesive damage consists of microscopic cracks that are parallel to the reference surface of the actuated plate and represent the early stages of a local delamination (or debonding) of the actuator.

The most striking difference between the LW1 and LW2 models is the predicted magnitude of the damage eigenvalues. The LW2 model predicts that the dominant damage eigenvalue (D_3) is almost twice as large as predicted by the LW1 model (see Part A of Figure 8). This increased growth of D_3 in the LW2 model is a direct consequence of explicitly including transverse normal strain and transverse normal stress which obtain very high tensile values near the free corner of the adhesive. Consequently, in the LW2 model, local damage evolution in the adhesive layer is driven by both transverse shear and transverse normal deformation, while the local adhesive damage in the LW1 model is driven only by transverse shear deformation. In contrast, the LW1 model predicts larger magnitudes for the non-dominant damage eigenvalues (D_1 and D_2) than the LW2 model. This last observation is due partly to the fact that the LW1 model inherently predicts slightly higher transverse shear deformation than the LW2 model, and partly due to the fact that the LW2 model's increased damage eigenvalue D_3 forces some of the shear forces to be redistributed, thus limiting the growth of D_1 and D_2.
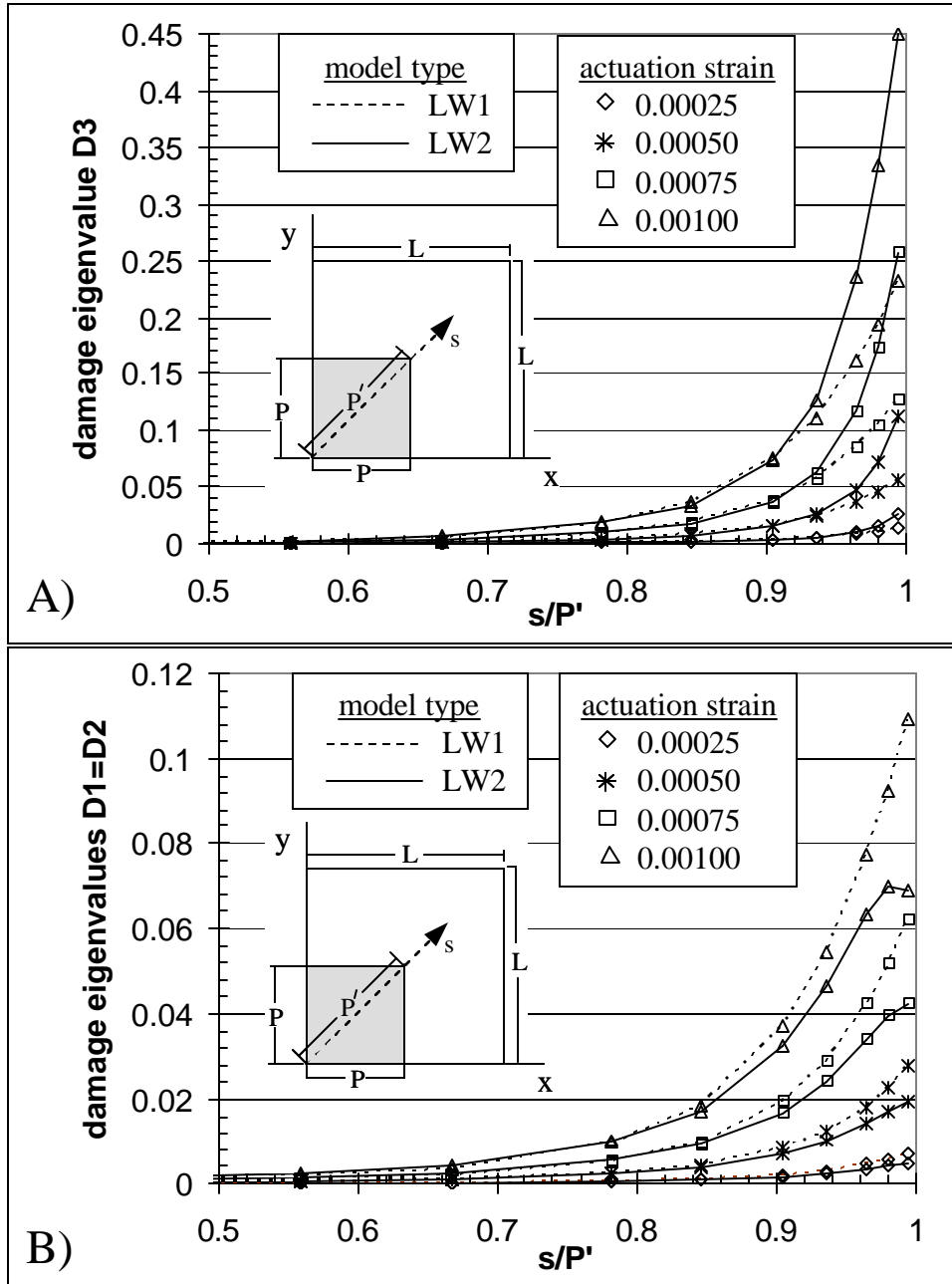
Figure 8. Comparison of damage distribution in the adhesive layer as predicted by LW1 and LW2 models for the case of bending actuation of a simply supported plate with $2P/H=2$ and $h_a/h=0.10$. Results are shown at four different actuation strain levels.
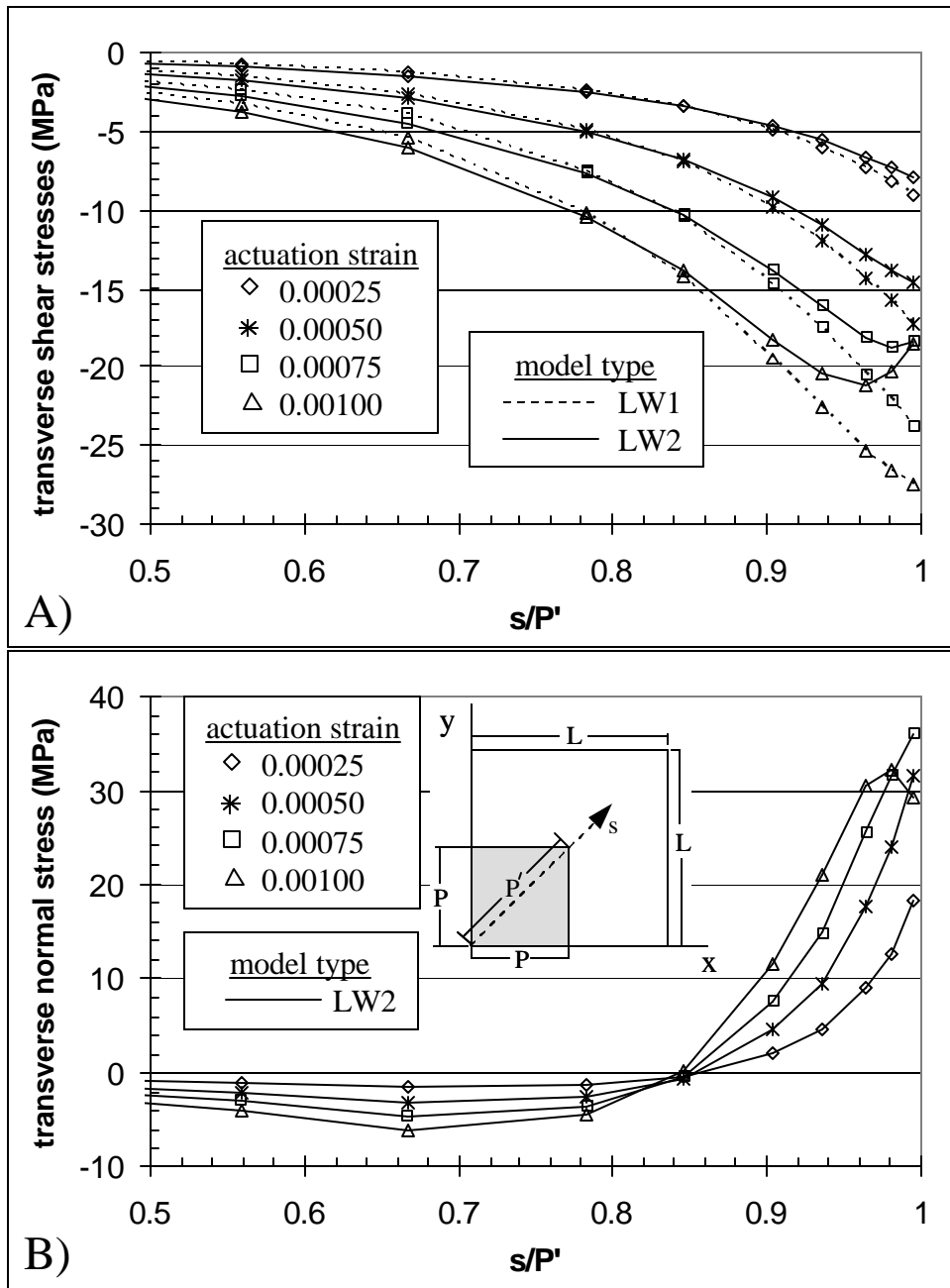
Figure 9. Comparison of stress distribution in the adhesive layer as predicted by LW1 and LW2 models for the case of bending actuation of a simply supported plate with 2P/H=2 and h_a/h=0.10. Results are shown at four different actuation strain levels.

Figure 9 shows the distribution of transverse shear stress and transverse normal stress in the damaged adhesive material of the thicker actuated plate (2P/H=2). In each case, the damaged stresses are computed only at the reduced Gaussian integration points within the adhesive material and are plotted along a diagonal line that runs from the center of the actuated region to the free corner of the actuator. Examination of Part A of Figure 9 reveals that the LW2 model predicts lower values of transverse shear stress than the LW1 model, especially at higher load levels. For low load levels (e.g. actuation strain ≤ 0.00025), the level of material damage is minimal; consequently, the difference between the LW1 and LW2 transverse shear stress is similar to that observed earlier for the linear elastic case. However, at high load levels (e.g. actuation strain ≥ 0.00075) the difference in predicted transverse shear stress is quite noticeable. This last observation is due primarily to the advanced state of damage (D_3) predicted by the LW2 model which severely limits the amount of transverse shear stress (see Part A) and transverse normal stress (see Part B) that the material can support.

For the thicker actuated plate (2P/H=2), Figure 10 shows the difference between the adhesive stresses obtained by linear elastic and progressive damage solutions using the LW1 and LW2 models. The stresses in Figure 10 are computed at the highest load level (actuation strain = 0.001). The linear elastic solutions show significant stress concentrations at the free corner of the adhesive, while the stresses obtained from the progressive damage solutions are limited in magnitude by the locally weakened state of the adhesive material.
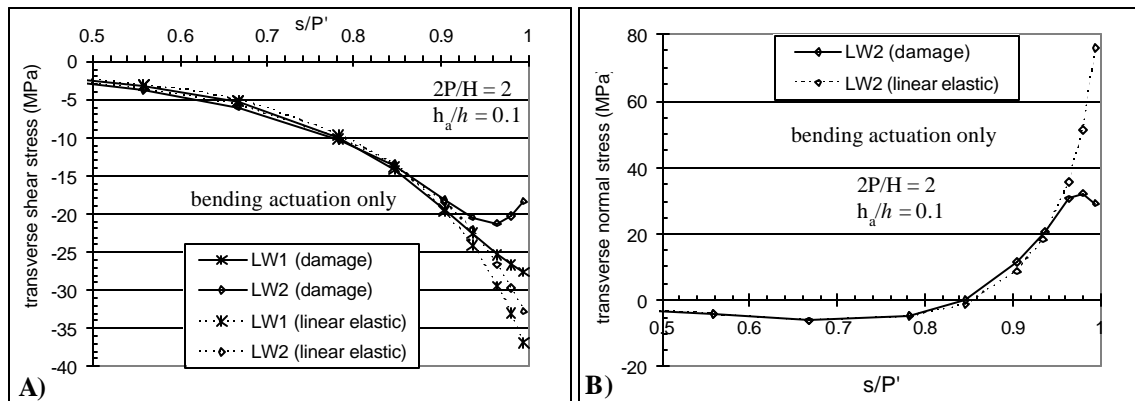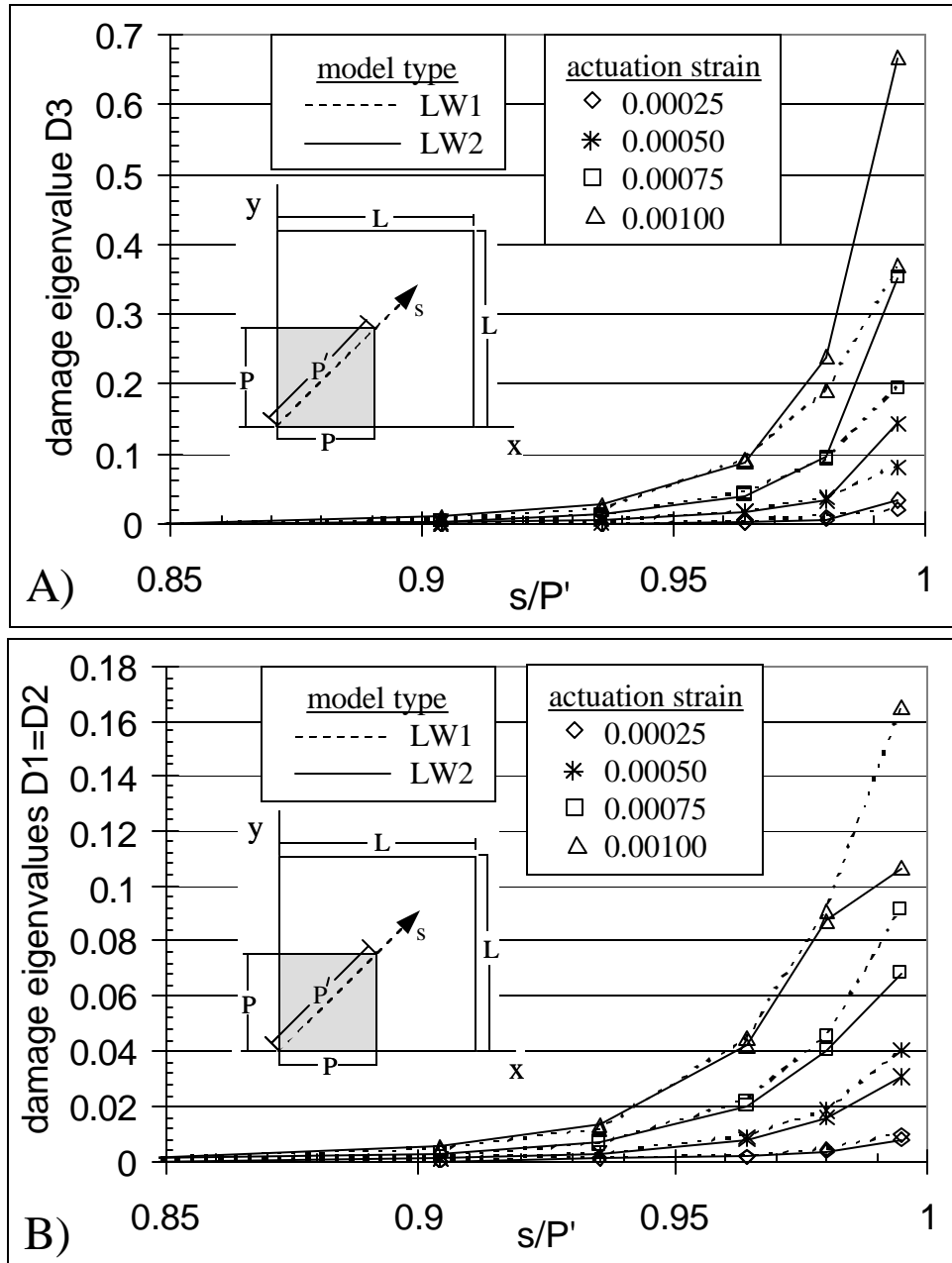

Figure 10. Comparison of stress distribution in the adhesive layer as predicted by linear elastic and progressive damage solutions obtained with LW1 and LW2 models. Results shown for a simply supported plate subjected to bending actuation (actuation strain = 0.001). 2P/H=2 and h_a/h=0.10.

Results for the thinner actuated plate (2P/H=8) are shown in Figures 10 through 12 and are entirely analogous to the previous Figures 7 through 9 respectively. The damage distributions shown in Figure 11 and the transverse stress distributions shown in Figure 12 show the same basic trends for the thinner actuated plate as observed earlier for the thicker actuated plate. Figure 13 shows a comparison between linear elastic and progressive damage solutions for the highest load level (actuation strain = 0.001). In comparing the results obtained for the two thickness configurations (2P/H=2 and

2P/H=8), the main difference is that the boundary layer region is much narrower for the thinner configuration; consequently, the boundary layer region of the thinner configuration is discretized with fewer elements than the thicker configuration, thus the damage and stress distributions seen in Figures 10 through 12 do not have the same degree of smoothness as seen earlier in Figures 7 through 9. However, despite the fact that fewer elements are used to resolve the boundary layer region in the thinner configuration, the predicted behavior is similar for both thickness configurations.

Figure 11. Comparison of damage distribution in the adhesive layer as predicted by LW1 and LW2 models for the case of bending actuation of a simply supported plate with 2P/H=8 and h_a/h=0.10. Results are shown at four different actuation strain levels.
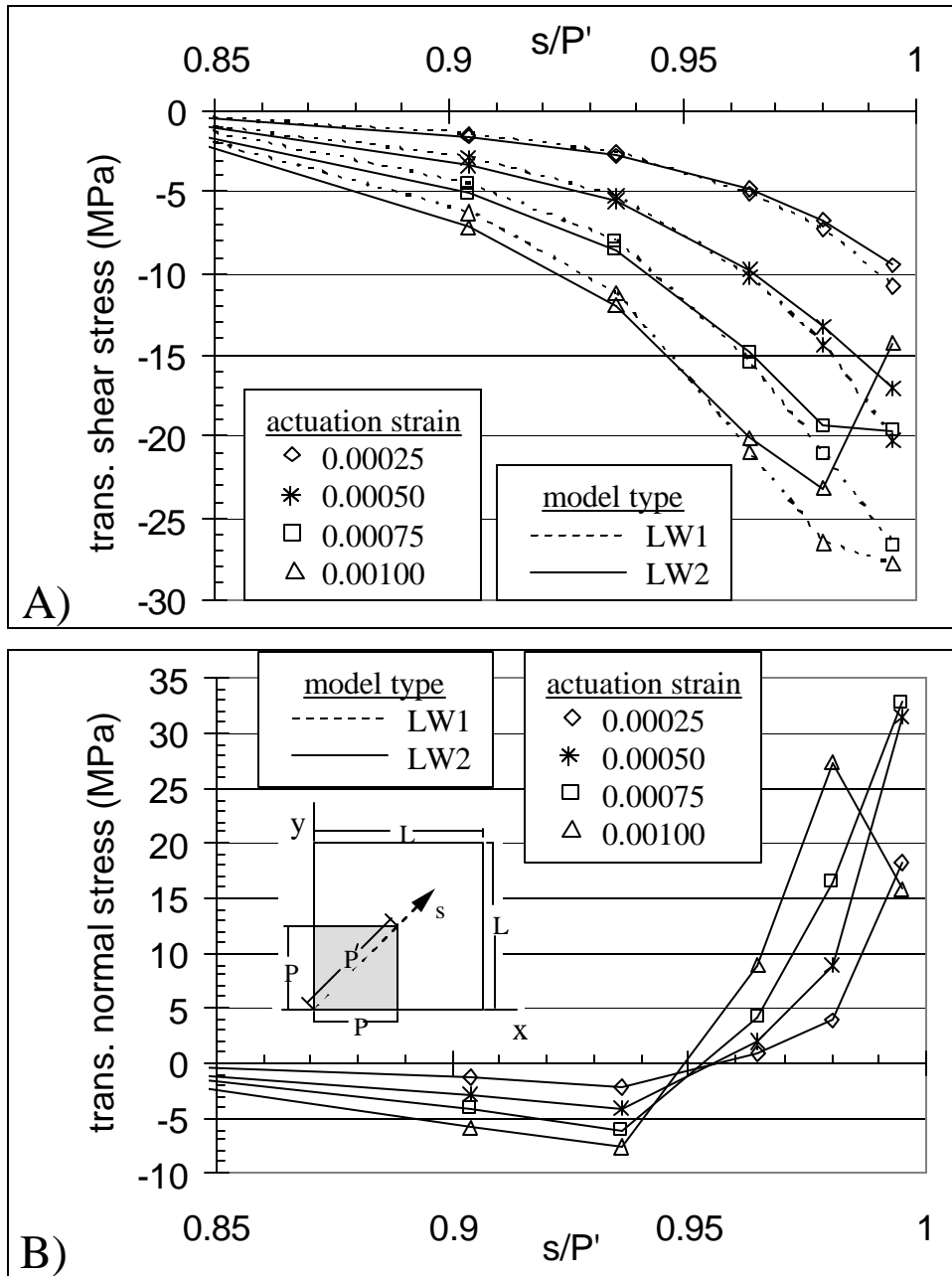
Figure 12. Comparison of stress distribution in the adhesive layer as predicted by LW1 and LW2 models for the case of bending actuation of a simply supported plate with 2P/H=2 and h_a/h=0.10. Results are shown at four different actuation strain levels.
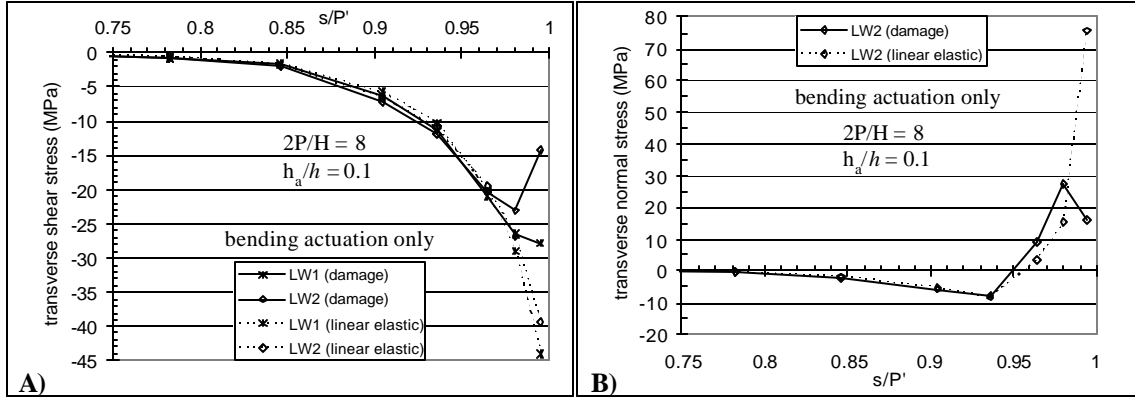
Figure 13. Comparison of stress distribution in the adhesive layer as predicted by linear elastic and progressive damage solutions obtained with LW1 and LW2 models. Results shown for a simply supported plate subjected to bending actuation (actuation strain = 0.001). $2P/H=8$ and $h_a/h=0.10$.

Finally, let us consider the effect of local adhesive damage on the ability of the actuators to produce global deformation in the actuated plate. Table 1 shows the predicted normalized center deflection of the simply supported plate under bending actuation (imposed actuation strain = 0.001). The center deflections are obtained from both linear elastic solutions and progressive damage solutions using both layerwise model types and both thickness configurations. Examination of the values in Table 1 reveals that, for all cases considered, the localized adhesive damage reduces the center deflection by less than 1%. Thus it is concluded that, although the adhesive damage is locally severe, it is not pervasive enough to seriously degrade the overall effectiveness of the actuators.

model type	2P/H	imposed actuation strain	solution type	center deflection $w(0,0,0)/h_P$	% difference in $w(0,0,0)$ (damage vs. elastic)
LW1	2	0.001	progressive damage	-0.002485	
LW1	2	0.001	linear elastic	-0.002502	0.67
LW2	2	0.001	progressive damage	-0.002431	
LW2	2	0.001	linear elastic	-0.002450	0.80
LW1	8	0.001	progressive damage	-0.045378	
LW1	8	0.001	linear elastic	-0.045436	0.13
LW2	8	0.001	progressive damage	-0.044967	
LW2	8	0.001	linear elastic	-0.045035	0.15

Table 1. Comparison of center deflection as influenced by model type, solution type and thickness configuration.

5.3 Progressive adhesive damage (bending actuation plus transverse loading)

The previous example considered damage to the adhesive bond layers that resulted from bending actuation alone, without any other form of mechanical loading. It was

demonstrated that an imposed actuation strain of 0.001 was sufficient to produce significant damage in the adhesive bond, but this damage was limited to the boundary layer region where very high values of transverse shear stress and transverse normal stress occur. It was further demonstrated that although the predicted adhesive damage was locally quite severe, the adhesive damage was not pervasive enough to significantly reduce the effectiveness of the actuators. In this section, we consider a more severe two-stage loading of the simply supported plate. More precisely, the plate is first loaded by a high level of bending actuation. Then, while holding the bending actuation constant, the plate is subjected to a uniform distributed transverse load that opposes the bending actuation. The magnitude of the uniform distributed load is incrementally increased until it effectively cancels the global deformation caused by the bending actuation. This results in a plate that exhibits minimal global deformation, but high stress levels.

Two different thickness configurations are considered (2P/H=2 and 2P/H=8). In each case, the adhesive layer thickness is 10% of the actuator thickness (h_a/h=0.1), while the actuator thickness is 25% of the aluminum plate thickness (h/H=0.25).   In each case, the constant bending actuation is brought about by applying an electric field that is sufficient to cause inplane normal strains of $\varepsilon_1=\varepsilon_2$=0.001 in an unconstrained piezoceramic patch. Note that this is equivalent to the maximum level of bending actuation imposed in the previous example; therefore, solutions for the present problem are computed by 're-starting' the previous solutions with the addition of a uniform distributed transverse load. For the thicker configuration (2P/H=2), the magnitude of the uniform distributed transverse load is increased in increments of 1 MPa until the loading is sufficient to cancel the bending actuation.   For the thinner configuration (2P/H=8), the magnitude of the uniform distributed transverse load is increased in increments of 0.0625 MPa until the loading is sufficient to cancel the bending actuation. For both cases, solutions are computed using both the LW1(2L/1L/4L) and LW2(2L/1L/4L) models on the 12x12g 2-D mesh.

Figure 14 shows the center deflection of the simply supported plate at each loadstep, where loadstep 0 corresponds to the application of bending actuation (imposed actuation strain = 0.001) without any distributed transverse load. In each subsequent loadstep, the opposing uniform distributed transverse load is increased by 1 MPa for the thicker configuration (2P/H=2), or 0.0625 MPa for the thinner configuration (2P/H=8). For comparison, both linear elastic solutions and progressive damage solutions are obtained using the LW1 model and the LW2 model. Part A of Figure 14 shows that, for the thicker configuration, a uniform distributed transverse load of approximately 4 MPa is required to cancel the global bending caused by the initial bending actuation. Furthermore, it is noticed that the overall load-deflection curves appear to be linear for both the LW1 and LW2 models despite the fact that local adhesive damage continues to accumulate with each loadstep. However, the slope of the load-deflection curve is shallower for the LW2 than for the LW1 model. For the thinner configuration, Part B of Figure 14 shows that a uniform distributed transverse load of approximately 0.375 MPa is required to cancel the global bending caused by the initial bending actuation. In this case, the load-deflection curves of the LW1 and LW2 models are indistinguishable from each other.
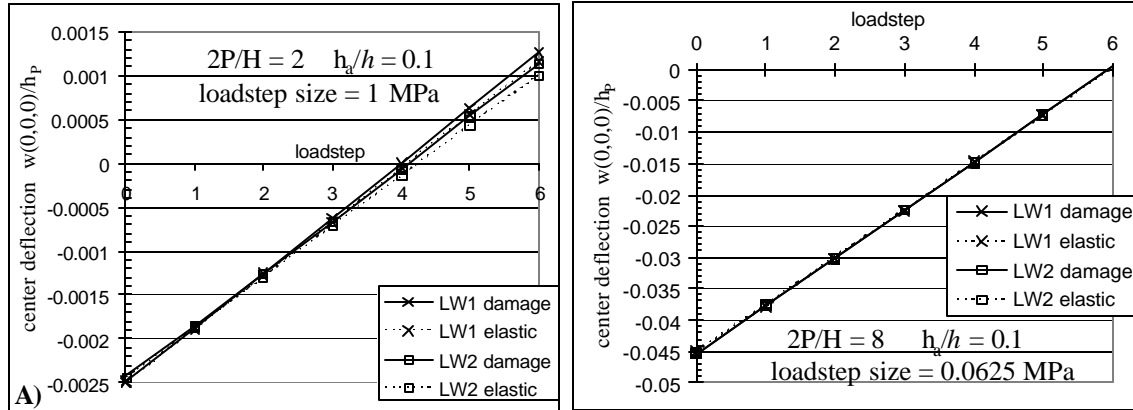
Figure 14. Normalized center deflection produced by constant bending actuation (actuation strain = 0.001) followed by an opposing uniform distributed transverse load.

For the thicker actuated plate configuration (2P/H=2), Figure 15 shows the evolution of local adhesive damage that occurs as the distributed load is increased from 0 MPa to 6 MPa. Specifically, Parts A and B of Figure 15 show the evolution of damage eigenvalues D_3 and $D_1=D_2$ respectively as predicted by the LW1 model. Parts C and D of Figure 15 show the evolution of the damage eigenvalues D_3 and $D_1=D_2$ respectively as predicted by the LW2 model. Examination of Figure 15 reveals several noteworthy trends. First, both models predict that the dominant form of damage consists of distributed microcracks that are oriented perpendicular to the transverse direction (characterized by D_3); however, the LW2 model predicts significantly higher values of D_3 than the LW1 model. In fact, if the distributed load is increased beyond 6 MPa (i.e. beyond loadstep 6), the LW2 model predicts a local delamination failure ($D_3=1$) at the reduced Gauss point closest to the free corner of the adhesive. Again, the LW2 model's larger values of D_3 can be explained by the fact that the LW2 model explicitly includes transverse normal stress which is a significant contributor to D_3 in this particular problem. Second, despite the fact that the LW2 model predicts higher values of D_3, both models predict approximately the same growth rate of D_3 as the distributed load is incremented. For example, over the course of six distributed load increments, both models show that the peak value of D_3 is approximately doubled. Third, the LW1 model predicts larger peak values of the non-dominant damage eigenvalues (D_1 and D_2) than the LW2 model; moreover, the two models predict qualitatively different evolution characteristics for these non-dominant damage eigenvalues. The LW1 model predicts that D_1 and D_2 continue to exhibit an ever-increasing maxima at the free corner of the adhesive. In contrast, the LW2 model predicts that the D_1 and D_2 maxima begin to move inward, away from the free corner of the adhesive as D_3 continues to increase.

Figure 16 shows the evolution of the local transverse stress components in the adhesive layer of the thicker configuration (2P/H=2) as the distributed load is increased from 0 MPa to 6 MPa. Specifically, Part A of Figure 16 shows the evolution of the transverse shear stress components $\sigma_{xz}=\sigma_{yz}$ as predicted by the LW1 model. Parts B and C of Figure 16 show the evolution of the transverse shear stress components and the transverse normal stress component respectively as predicted by the LW2 model. Examination of Parts A-C of Figure 16 reveals that as local damage accumulates near the free corner of the adhesive, local load redistribution occurs; i.e., the portion of the stress

35

that can not be supported by the damaged material is transferred to neighboring material that is less damaged. In Parts A-C of Figure 16, as the distributed load is increased, the location of the transverse stress maxima shifts to the left into lesser damaged material. At the same time, the stress near the free corner of the adhesive decreases commensurate with the increasing level of local damage. Also, it is noted that within any particular plot (A, B, or C), the peak stress value remains constant as the stress distribution shifts to the left (at least to the extent that the chosen mesh can resolve the stress field). This constant peak stress is consistent with a material that can only support a limited level of stress for any given deformation state. Interestingly, the LW2 model predicts that the adhesive material can support a maximum transverse shear stress of $\sigma_{xz}=\sigma_{yz}=22.5$ MPa, while the LW1 model predicts that the adhesive material can support a maximum transverse shear stress of $\sigma_{xz}=\sigma_{yz}=27.5$ MPa. It should be noted that the exact same damage evolution equations are used in both models; thus, the difference in peak shear stress is caused by the fact that the LW2 model predicts more of a local triaxial state of stress than the LW1.
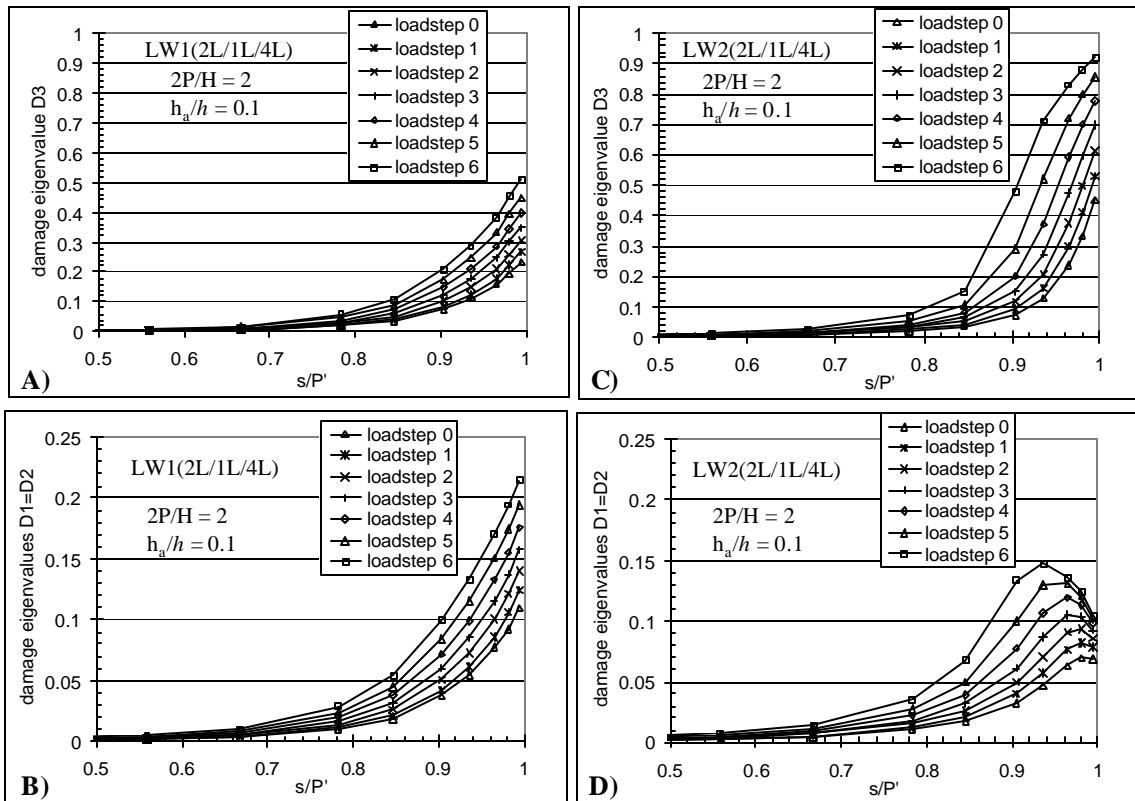

Figure 15. Comparison of damage distribution in the adhesive layer as predicted by LW1 model (Parts A & B) and LW2 model (Parts C & D). Uniform distributed transverse load increments (1 MPa each) are applied to oppose pre-existing bending actuation (actuation strain = 0.001).
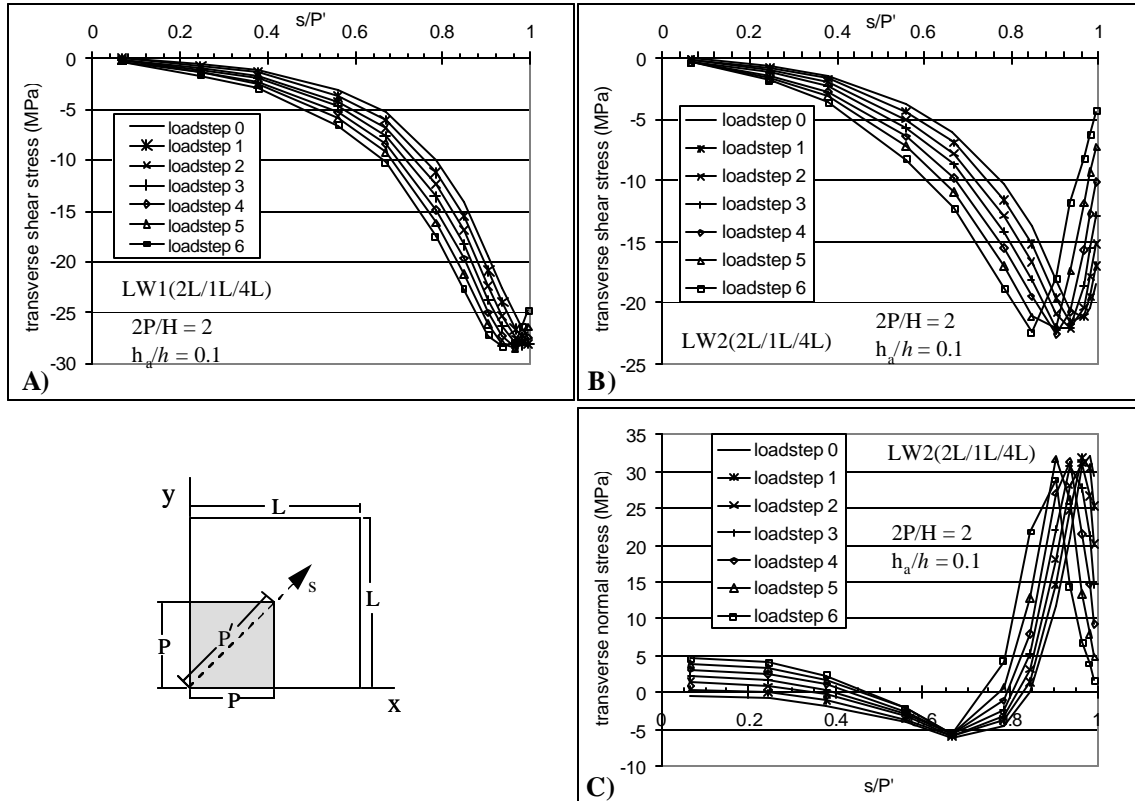
Figure 16. Comparison of stress distribution in the adhesive layer as predicted by LW1 and LW2 models. Uniform distributed transverse load increments (1 MPa) are applied to oppose pre-existing bending actuation (actuation strain = 0.001). 2P/H=2, h_a/h=0.10.

For the thicker actuated plate configuration (2P/H=2), Figure 17 shows the distribution of transverse stresses in the adhesive layer at a distributed load of 4 MPa. This particular level of transverse loading is just sufficient to counteract the imposed bending actuation. The stresses in Figure 17 are obtained from progressive damage solutions and linear elastic solutions using both the LW1 and LW2 models. As seen in Figure 17, the linear elastic solutions predict significant transverse stress concentrations near the free corner of the adhesive. In the progressive damage solutions, these transverse stress concentrations can not be tolerated and result in adhesive damage which severely limits the magnitude of the local transverse stresses.
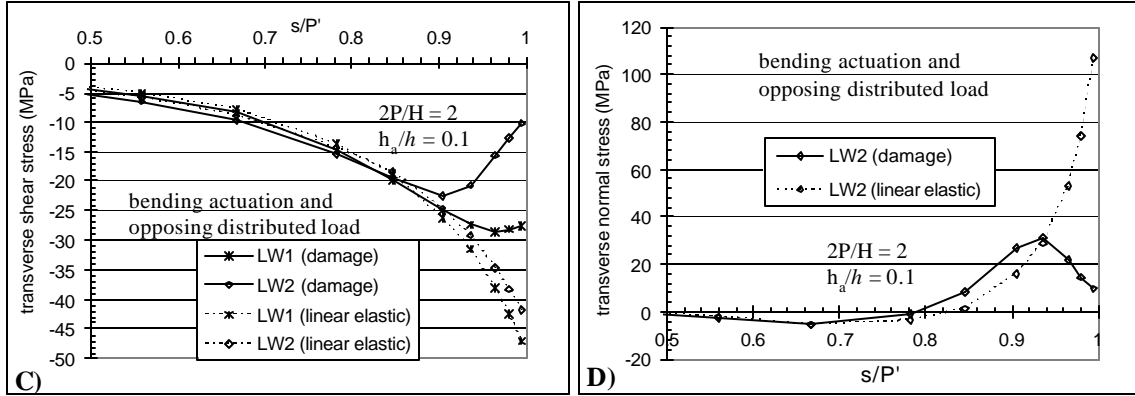
Figure 17. Comparison of stress distribution in the adhesive layer as predicted by linear elastic and progressive damage solutions obtained with LW1 and LW2 models. Results shown for a simply supported plate subjected to combined bending actuation (actuation strain = 0.001) and opposing uniform distributed transverse load (4 MPa). 2P/H=2 and h_a/h=0.10.

Results for the thinner actuated plate configuration (2P/H=8) are shown in Figures 17 through 19 which are entirely analogous to earlier Figures 14 through 16 respectively. Figures 17 and 18 show the distribution of damage eigenvalues and damaged transverse stresses predicted by the LW1 and LW2 models for the thinner configuration (2P/H=8) and show the same general trends discussed earlier for the thicker configuration. Figure 20 shows a comparison between linear elastic and progressive damage solutions at a uniform distributed transverse load of 0.375 MPa. This particular level of transverse loading is just sufficient to counteract the imposed bending actuation (actuation strain = 0.001). In comparing the results obtained for the two thickness configurations(2P/H=2 and 2P/H=8), the main difference is that the boundary layer region is much narrower for the thinner configuration; consequently, the boundary layer region of the thinner configuration is discretized with fewer elements than the thicker configuration, thus the damage and stress distributions seen in Figures 17 through 19 do not have the same degree of smoothness as seen earlier in Figures 14 through 16. However, despite the fact that fewer elements are used to resolve the boundary layer region in the thinner configuration, the predicted behavior is similar for both thickness configurations.
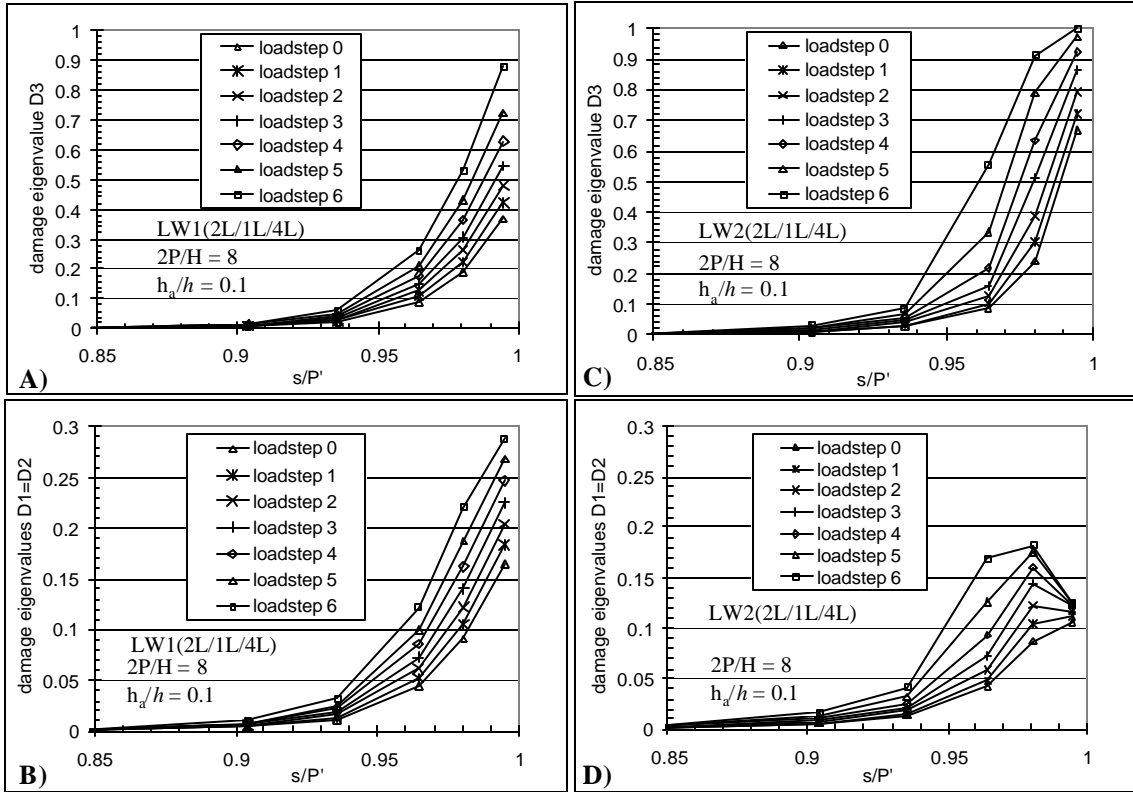
Figure 18. Comparison of damage distribution in the adhesive layer as predicted by LW1 and LW2 models. Uniform distributed transverse load increments (0.0625 MPa) are applied to oppose pre-existing bending actuation (actuation strain = 0.001). 2P/H=8, h_a/h=0.10.
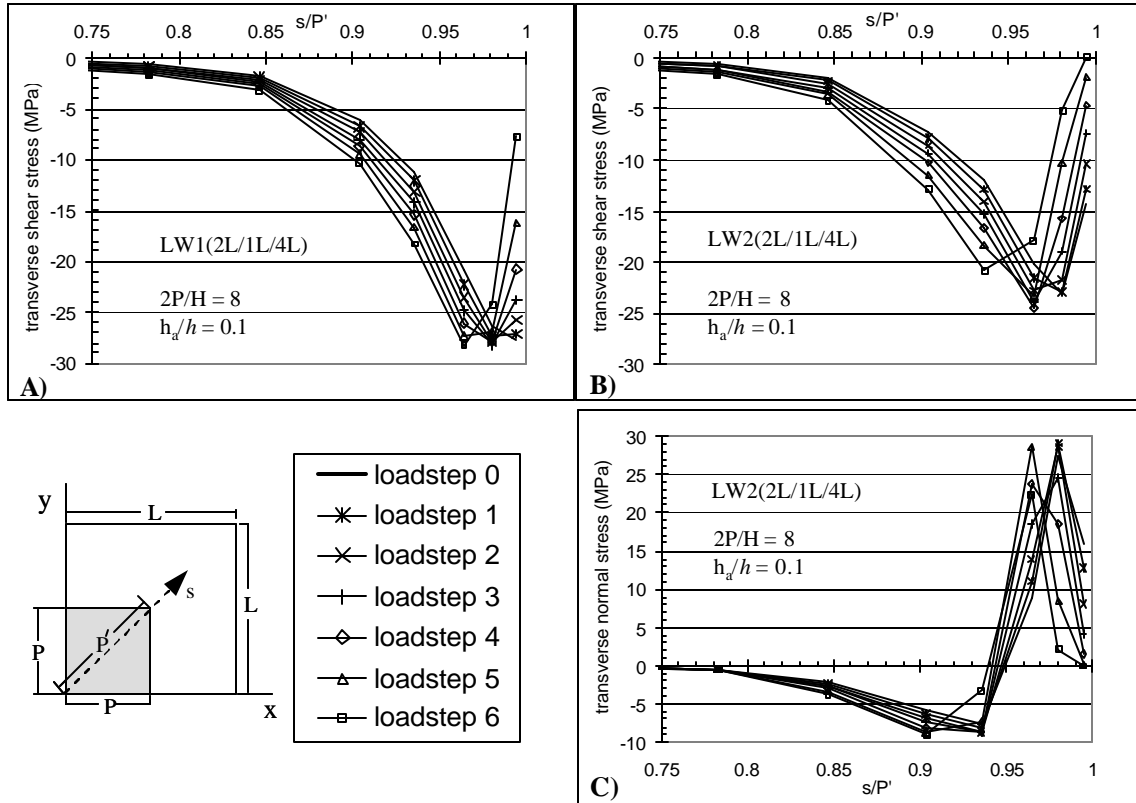
Figure 19. Comparison of stress distribution in the adhesive layer as predicted by LW1 and LW2 models. Uniform distributed transverse load increments (0.0625 MPa) are applied to oppose pre-existing bending actuation (actuation strain = 0.001). 2P/H=8, h_a/h=0.10.
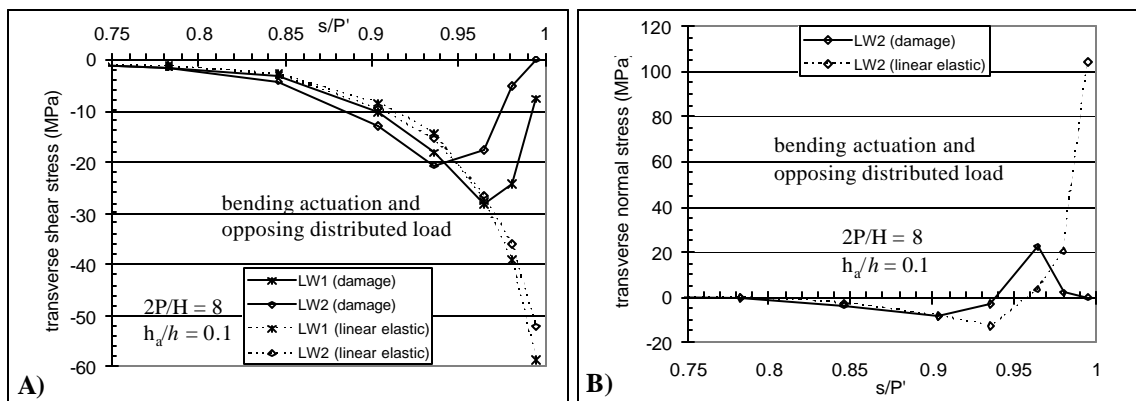

Figure 20. Comparison of stress distribution in the adhesive layer as predicted by linear elastic and progressive damage solutions obtained with LW1 and LW2 models. Results shown for a simply supported plate subjected to combined bending actuation (actuation strain = 0.001) and opposing uniform distributed transverse load (0.375 MPa). 2P/H=8 and h_a/h=0.10.

5.4 Progressive adhesive damage (distributed transverse loading only)

As a final example, let us consider the evolution of local adhesive damage that occurs as the actuated plate is subjected to a uniform distributed transverse load without any electrical field applied to the actuators. Again, two different thickness configurations are considered (2P/H=2 and 2P/H=8). In each case, the adhesive layer thickness is 10% of the actuator thickness (h_a/h=0.1), while the actuator thickness is 25% of the aluminum plate thickness (h/H=0.25).   In both cases, the uniform distributed transverse load is applied to the bottom surface of the actuated plate and acts in an upward direction. For the thicker configuration (2P/H=2), the magnitude of the uniform distributed transverse load is increased in increments of 1 MPa until the loading is sufficient to initiate a localized material failure in one of the adhesive layers. For the thinner configuration (2P/H=8), the magnitude of the uniform distributed transverse load is increased in increments of 0.0625 MPa until the loading is sufficient to initiate a localized material failure in one of the adhesive layers. For both cases, solutions are computed using the LW2(2L/1L/4L) model on the 12x12g 2-D mesh.

For the thicker configuration (2P/H=2), the initial material failure occurred at a load of 15 MPa, while the thinner configuration exhibited the initial material failure at a load of 1.3125 MPa. In both cases, the initial material failure occurred at the reduced Gauss point located closest to the free corner of the lower adhesive layer and was indicative of a delamination initiation, or debonding (i.e. D_3=1). Figure 21 shows the distribution of the damage eigenvalues and the distribution of the transverse stresses that occur in the lower adhesive layers of both configurations during the loadstep immediately preceding the initial localized adhesive failure. Examination of Parts A and C of Figure 21 reveals that the adhesive damage is primarily characterized by a high concentration of microcracks that are oriented perpendicular to the thickness direction (i.e., D_3>>D_1=D_2). Both thickness configurations exhibit damage distributions with similar shapes and similar ratios between the various damage eigenvalues. The main difference is simply the width of the boundary layer where significant adhesive damage occurs. Parts B and D of Figure 21 show the distribution of the transverse stresses that occur in the lower adhesive layers of both configurations. In order to emphasize the local load redistribution that occurs as damage accumulates near the free corner of the adhesive, Parts B and D of Figure 21 also show the distribution of the transverse stresses predicted by linear elastic (non-damaging) solutions. A comparison of these stress distributions shows that the linear elastic stress concentrations are completely absent in the progressive damage solution.
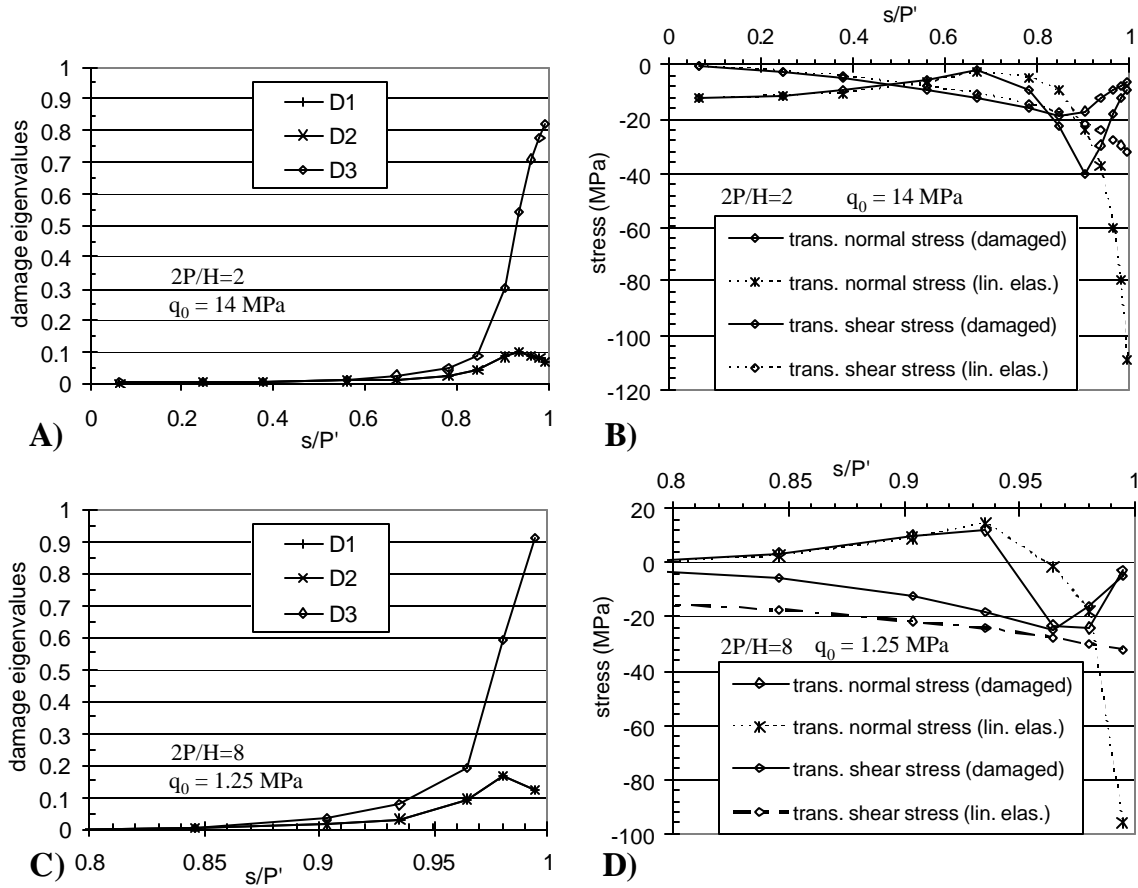
Figure 21. Damage and transverse stress distribution in the lower adhesive bond layer for simply supported actuated plate subjected to uniform distributed transverse load with passive actuators.

Finally, let us consider the effect of local adhesive damage on the overall structural stiffness of the actuated plate. In the present example problem, the actuators are passive; therefore, the actuators simply provide an additional bending stiffness to the aluminum plate. However, if the adhesive bond layers are damaged, then the aluminum plate is effectively prevented from utilizing all of the extra stiffness provided by the actuators; consequently, the actuated plate exhibits increased overall compliance. To quantify this effect, Table 2 shows the transverse center deflection $w(0,0,0)$ predicted for both configurations by linear elastic solutions and progressive damage solutions. As seen in Table 2, the center deflections are larger for the progressive damage solutions than for the linear elastic solutions; however, the increase in overall bending compliance is quite small. For the thicker configuration, the damaged adhesive layer allows a 1.4% increase in center deflection. For the thinner configuration, the damaged adhesive layer only allows a 0.7% increase in center deflection.   Thus, while the adhesive damage is locally quite severe (see Parts A and C of Figure 21), the damage is not pervasive enough to significantly degrade the stiffness support function of the actuators.

model type	2P/H	trans. load (MPa)	solution type	center deflection w(0,0,0)/h$_P$	% difference in w(0,0,0) (damage vs. elastic)
LW2	2	14	linear elastic	0.008252	
LW2	2	14	prog. damage	0.008369	1.4%
LW2	8	1.25	linear elastic	0.15061	
LW2	8	1.25	prog. damage	0.15165	0.7%

Table 2. Comparison of center deflections obtained by linear elastic solutions and progressive damage solutions.

6. Summary and Conclusions

This paper presented a 3-D continuum damage mechanics formulation and described its numerical implementation into a hierarchical, variable-kinematic finite element model that is specifically developed for composite laminates.   The damage eigenvalues represent the effective fractional reduction in load carrying area on planes that are perpendicular to the principal material directions (i.e., orthotropic damage) and are permitted to exhibit a spatial variation within each material ply that is commensurate with the predicted ply-level strain fields. The resulting model was used to simulate the accumulation of microscopic damage in the adhesive bond layers of a simple actuated plate (up to the point of initial material failure in the adhesive).   Solutions were obtained using both type-I and type-II layerwise finite elements for simply-supported actuated plates subjected to bending actuation and/or distributed transverse loading.

The results obtained for the actuated plate problem clearly show that, even under very mild levels of external loading, the high concentration of transverse shear strain and transverse normal strain that exists near the free edges of the adhesive layer leads to the initiation of localized adhesive damage. This damage manifests itself primarily in the form of distributed microcracks that are oriented normal to the transverse direction and was shown to be most severe at the free corners of the adhesive layer. As the external loading is increased, the localized damage within the adhesive boundary layer becomes quite severe and can easily lead to local material failure; however, due to the limited size of the damaged region, the degradation of overall actuator function was shown to be minimal. In addition, the damage to the adhesive layer did not significantly impair the stiffness support function of the actuators when operating in passive mode.

A comparison of solutions obtained from type-I and type-II layerwise models showed that the LW2 model predicted significantly higher values of local adhesive damage than the LW1 model. Therefore, it can be concluded that transverse normal strain is a significant contributor to local damage accumulation in adhesive layer. Thus the prediction of damage accumulation in the adhesive layer is shown to require the use of a full 3-D macroscopic model that explicitly accounts for all six strain components on a discrete layer basis.

7. References

Allen, D. H., Harris, C.E. and Groves, S.E. 1987. "A Thermomechanical Constitutive Theory For Elastic Composites With Distributed Damage - Part I: Theoretical Development," *International Journal of Solids and Structures*, 23(9):1301-1318.

Allen, D.H., Harris, C.E. and Groves, S.E., "A Thermomechanical Constitutive Theory For Elastic Composites With Distributed Damage - Part II: Application To Matrix Cracking In Laminated Composites," *International Journal of Solids and Structures*, 23(9):1319-1338.

Allix, O. and Ladeveze, P. 1989. "A Damage Prediction Mehtod For Composite Structures," *International Journal for Numerical Methods in Engineering*, 27:271-283.

Allix, O. and Ladeveze, P. 1992. "Interlaminar Interface Modelling For The Prediction Of Laminate Delamination," *Composite Structures*, 22:235-242.

Barbero, E. and De Vivo, L. 2001. "A Constitutive Model For Elastic Damage In Fiber-Reinforced PMC Laminae," *International Journal of Damage Mechanics*, 10:73-93.

Barbero, E. and Lonetti, P. 2002. "An Inelastic Damage Model For Fiber Reinforced Laminates," *Journal of Composite Materials*, 36(8):941-962.

Benjeddou, A. 2000. "Advances In Piezoelectric Finite Element Modeling Of Adaptive Structural Elements: A Survey," *Computers and Structures*, 76:347-363.

Chattopadhyay, A., Li, J. and Gu, H. 1999. "Coupled Thermo-Piezoelectric-Mechanical Model for Smart Composite Laminate," *AIAA Journal*, 37(12):1633–16389.

Chopra, I., "Review of State of Art of Smart Structures and Integrated Systems," *AIAA Journal*, Vol. 40, No. 11, pp. 2145-2187, 2002.

Cordebois, J.P. and Sidoroff, F. 1982. "Damage Induced Elastic Anisotropy," in *Mechanical Behavior of Anostropic Solids*, J.P. Boehler (ed), Martinus Nijhoff, Boston, pp.761-774.

Crawley, E.G. and de Luis, J. 1987. "Use of Piezoelectric Actuators as Elements of Intelligent Structures," *AIAA Journal*, 25:1373-1385.

Dragon, A. 2002. "Continuum Damage Mechanics Applied to Quasi-Brittle Materials," *Continuum Damage Mechanics of Materials and Structures*, Eds. O. Allix and F. Hild, Elsevier, Amsterdam, pp. 165-204.

Gopinathan, S.V., Varadan, V.V. and Varadan, V.K. 2000. "A Review and Critique of Theories for Piezoelectric Laminates," *Smart Materials and Structures*, 9:24–48.

Heyliger, P., Ramirez, G. and Saravanos, D.A. 1994. "Coupled Discrete Layer Finite Elements for Laminated Piezoelectric Plates," *Communications in Numerical Methods in Engineering,* 10:971–981.

Heyliger, P. 1997. "Exact Solutions for Simply Supported Laminated Piezoelectric Plates," *Journal of Applied Mechanics*, 64:299–306.

Kim, S.J. and Jones, J.D. 1996. "Effects of Piezo-Actuator Delamination on the Performance of Active Noise and Vibration Control Systems," *Journal of Intelligent Material Systems and Structures*, 7(6):668-676.

Krajcinovic, D. 1996. *Damage Mechanics*, North Holland, Amsterdam.

Ladeveze, P. 2002. "An Anisotropic Damage Theory with Unilateral Effects: Applications to Laminates and to Three- and Four-Dimensional Composites,"

Continuum Damage Mechanics of Materials and Structures, Eds. O. Allix and F. Hild, Elsevier, Amsterdam, pp. 205-234.

Ladeveze, P., Allix, O., Deu, J-F. and Leveque, D. 2000. "A mesomodel for localisation and damage computation in laminates, *Computer Methods in Applied Mechanics and Engineering*, 183:105-122.

Ladeveze, P. and Le Dantec, E. 1992. "Damage modeling of the elementary ply for laminated composites, *Composite Science and Technology*, 43(2):257-267, 1992.

Lee, C.K. 1990. "Theory of Laminated Piezoelectric Plates for the Design of Distributed Sensors/Actuators. Part I: Governing Equations and Reciprocal Relationships," *Journal of the Acoustic Society of America*, 87(3):1144-1158.

Lee, H., Peng, K. and Wang, J. 1985. "An Anisotropic Damage Criterion for Deformation Instability and its Application to Forming Limit Analysis of Metal Plates, *Engineering Fracture Mechanics*, 21:1031-1054.

Lee, H.J. and Saravanos, D.A. 1997. "Generalized Finite Element Formulation for Smart Multilayered Thermal Piezoelectric Composite Plates," *International Journal of Solids and Structures,* 34(26):3355-3371.

Lee, J.W., Allen, D.H. and Harris, C.E. 1989. "Internal State Variable Approach for Predicting Stiffness Reductions in Fibrous Laminated Composites with Matrix Cracks," *Journal of Composite Materials*, 23:1273-1291.

Lemaitre, J., 1996. *A Course on Damage Mechanics*, 2nd Ed., Springer, Berlin.

Lene, F. 1986. "Damage Constitutive Relations For Composite Materials," *Engineering Fracture Mechanics*, 25(5/6):713-728.

Lin, C.C., Hsu, C.Y. and Huang, H.N. 1996. "Finite Element Analysis on Deflection Control of Plates with Piezoelectric Actuators," *Composite Structures,* 35:423–33.

Lonetti, P., Zinno, R., Greco, F. and Barbero, E. 2003. "Interlaminar Damage Model For Polymer Matrix Composites," *Journal of Composite Materials*, 37(16):1485-1504.

Miller, S.E. and Abramovich, H. 1995. "A Self-Sensing Piezolaminated Actuator Model for Shells using a First Order Shear Deformation Theory," *Journal of Intelligent Material Systems and Structures*, 6:624–38.

Reddy, J.N. 1987. "A Generalization of Two-Dimensional Theories of Laminated Composite Plates," *Communications in Applied Numerical Methods*, 3:73-180.

Reddy, J.N. 1989. "On the Generalization of Displacement-Based Laminate Theories," *Applied Mechanics Reviews*, 42(11/Part 2):S213-S222.

Robbins, D.H.,Jr. and Reddy, J.N. 1991. "Finite Element Analysis of Piezoelectrically Actuated Beams," *Computers and Structures*, 41(2):265-279.

Robbins, D.H.,Jr. and Reddy, J.N. 1993. "Modelling of Thick Composites Using a Layerwise Laminate Theory," *International Journal for Numerical Methods in Engineering*, 36:655-677.

Robbins, D.H.,Jr. and Reddy, J.N. 1996. "An Efficient Computational Model for the Stress Analysis of Smart Plate Structures," *Smart Materials and Structures,* 5(3):353-360.

Robbins, D.H.,Jr. and Chopra, I. 2006. "The Effect Of Laminate Kinematic Assumptions On The Global Response Of Actuated Plates," to appear in *International Journal of Intelligent Materials and Structures*.

Robbins, D.H., Jr., Reddy, J.N. and Rostam-Abadi, F. 2005. "An Efficient Continuum Damage Model And Its Application To Shear Deformable Laminated Plates," *Mechanics of Advanced Materials and Structures*, 12(6):391-412.

Robbins, D.H., Jr. and Reddy, J.N. 2006. "Layerwise Modeling of Progressive Damage In Fiber-Reinforced Composite Laminates," to appear in *Mechanics of Advanced Materials and Structures*.

Saravanos, D.A. and Heyliger, P.R. 1995. "Coupled Layerwise Analysis of Composite Beams with Embedded Piezoelectric Sensors and Actuators," *Journal of Intelligent Material Systems and Structures*, 6(3):350-363.

Saravanos, D.A., Heyliger, P.R. and Hopkins, D.A. 1997. "Layerwise Mechanics and Finite Element for the Dynamic Analysis of Piezoelectric Composite Plates," *International Journal of Solids and Structures,* 34(3):359-378.

Saravanos, D.A. 1997. "Mixed Laminate Theory and Finite Element for Smart Piezoelectric Composite Shell Structures," *AIAA Journal*, 35:1327–33.

Skrzypek, J. and Ganczarski, A. 1999. *Modeling of Material Damage and Failure of Structures*, Springer, Berlin.

Sun, D., Tong, L. and Atluri, S.N. 2001. "Effects Of Piezoelectric Sensor/Actuator Debonding On Vibration Control Of Smart Beams," *International Journal of Solids and Structures*, 38(50-51):9033-9051.

Talreja, R. 1985. "A Continuum Mechanics Characterization Of Damage In Composite Materials," *Proceedings of the Royal Society* A399, pp. 195-216.

Tzou, H.S. and Gadre, M. 1989. "Theoretical Analysis of a Multi-Layered Thin Shell Coupled with Piezoelectric Shell Actuators for Distributed Vibration Controls," *Journal of Sound and Vibration*, 132(3): 433-450.

Vel, S.S. and Batra, R.C. 2000. "Cylindrical Bending of Laminated Plates with Distributed and Segmented Piezoelectric Actuators/Sensors**,"** *AIAA Journal*, 38(5):857-867.

Voyiadjis, G.Z. and Deliktas, B. 2000. "A Coupled Anisotropic Damage Model For The Inelastic Response Of Composite Materials, *Computer Methods in Applied Mechanics and Engineering*, 183:159-199.

Voyiadjis, G.Z. and Kattan, P.I. 1993. "Damage of fiber reinforced composite materials with micromechanical characterization," *International Journal of Solids and Structure*s, 30:2757-2778.

Voyiadjis, G.Z. and Kattan, P.I. 1999. *Advances in Damage Mechanics: Metals and Metal Matrix Composites*, Elsevier, Amsterdam.

Voyiadjis, G.Z. and Park, T. 1999. "Kinematics description of damage for finite strain plasticity, *Journal of Engineering Science*, 37:803-830.

Zhang, J. et al. 2003. "A Coupled Electromechanical Analysis Of A Piezoelectric Layer Bonded To An Elastic Substrate: Part I, Development Of Governing Equations," *International Journal of Solids and Structures*, 40:6781–6797.

Zhou, X., Chattopadhyay, A. and Gu, H. 2000. "Dynamic Response of Smart Composites Using a Coupled Thermo-Piezoelectric-Mechanical Model," *AIAA Journal*, 38(10):1939–1948.